Photofabrication of Color-Picture-Tube Shadow Masks: Etching Kinetics of Low-Carbon Steel, Process Design for Data-Display Masks, and the Etching of Invar

R. B. Maynard, J. J. Moscony, M. H. Saunders, E. E. Doerschuk and D. M. Weber — RCA Video Component and Display Division, Lancaster, PA 17604

Combined and edited from three 1984 papers and four RCA/Thomson patents, with editor's notes, by David F. Hakala, Ph.D., NanoTekniks

November 4, 2026

Note on this reconstruction

This paper combines three companion papers from the RCA Video Component and Display Division (VCDD) at Lancaster, both published in the spring of 1984:

- **[A]** E. E. Doerschuk, J. J. Moscony and D. M. Weber, "Shadow-mask etching for data-display tubes," *RCA Engineer* **29**-2, 67–73 (March/April 1984). This paper covers mask designs, steel selection, aperture geometry and the etching process.
- **[B]** R. B. Maynard, J. J. Moscony and M. H. Saunders, "Ferric Chloride Etching of Low Carbon Steels," *RCA Review* **45**, 73–89 (March 1984). This paper covers the etching chemistry and kinetics in the production etchant.
- **[C]** R. B. Maynard, J. J. Moscony and M. H. Saunders, "A Study of the Etching Kinetics of Low Carbon Steel Using the Ferric Perchlorate–Perchloric Acid System as a Model," *RCA Review* **45**, 58–72 (March 1984). This paper uses a simplified etchant, followed by UV spectrophotometry, to establish the transport-limited mechanism.

Section 5.3 also draws on the patent covering the precision-etch equipment, D. M. Weber and R. A. Alleman, US 4,389,279 (1983) [3], for its design details and test data (Table 13).

Section 6, on Invar masks, was added in 2026. It draws on two later patents by the same Lancaster group, R. B. Maynard, J. J. Moscony and M. H. Saunders, US 4,482,426 (1984) [26], and J. J. Moscony and B. M. Cushman, US 5,718,874 (1998) [27], and on a 2017 paper on spray etching thin Invar foil [32].

The text of all three papers is retained, retyped from scanned copies, corrected for character-recognition errors and arranged in one sequence: mask designs, the photofabrication process, steel, etch chemistry (first the perchlorate model system, then ferric chloride), and finally aperture geometry and etch-process design. Linking sentences were added where needed, and figures, tables and references were renumbered. Figure 7 of [A] is the same as Fig. 9 of [B] and appears once (Fig. 23). The footnotes of [C] are folded into the text and reference list. Section 2.1 is an editor's outline of the standard photofabrication sequence, which none of the papers describes in full, and is marked as such. SI equivalents are given in brackets after U.S. customary units. Figure E1 and the Editor's Notes at the end were added in 2026; they include a cross-check of the two kinetic studies against each other (Note 6).

Abstract

The shadow mask of a high-resolution data-display color picture tube carries three times as many apertures per unit area as the mask of a conventional entertainment tube. Its apertures are formed by photolithography and spray etching of thin low-carbon steel strip in acidified ferric chloride. This paper reports the metallurgical and process changes RCA made to produce such masks, together with a study of the underlying etch kinetics, first in a ferric perchlorate model system and then in the production ferric chloride etchant. Aluminum-killed steel replaced rimmed steel. It has lower and more uniformly distributed impurities, so it gives cleaner aperture edges, and it can be annealed free of yield-point elongation, so the mask forms more uniformly. In the model system, loss of ferric hexaaquo ion is first order in Fe^{3+}, proportional to steel area, inversely dependent on solution volume and viscosity, increased by stirring and unaffected by ferrous ion, with $\Delta H‡ \approx 2.8$ kcal/mol [12 kJ/mol]: the rate is limited by the encounter of Fe^{3+} with the steel surface. Beaker etching of 1008 rimmed steel in ferric chloride–hydrochloric acid shows transport-limited kinetics at low Baumé (below about 40° Bé; $\Delta H‡ = +3.07 \pm 0.13$ kcal/mol [12.8 kJ/mol]) and surface-limited kinetics at high Baumé (above about 54° Bé; $\Delta H‡ = +10.9 \pm 0.5$ kcal/mol [45.6 kJ/mol]). Added chloride inhibits etching, most strongly at high Baumé, consistent with the growing role of the $FeCl_4^-$ complex. Surface roughness rises abruptly, from about 6–7 microinches [0.15–0.18 µm] to over 25 microinches [0.64 µm], when the Baumé falls below a transition value that increases with temperature. Operating in the smooth-etch region, increasing the share of etching from the screen side before breakthrough, and, for the finest masks, a two-step "precision" etch with a shielded first stage produced data-display masks of good uniformity. A section added in 2026 extends the account to Invar (Fe–36Ni) masks from later RCA and Thomson patents: nickel ion accumulating in the etchant slows etching and raises the Baumé needed for a smooth finish, so production etching is held at 70–85 °C, 48–51° Bé and no more than 5 mol% nickel, with the spent etchant regenerated by solvent extraction of iron as $FeCl_4^-$.

1. Introduction

Since the beginning of commercial color television in 1950, the shadow-mask color picture tube has been the overwhelming choice of receiver manufacturers as the display medium for transmitted TV signals. Over the years, color picture tubes have undergone many improvements. In the newly designed color picture tubes, the shadow mask itself has evolved steadily to more complex designs that have kept pace with the growing need for better tube contrast, beam convergence and focus. These requirements have also called for equipment improvements involving capital investment of many millions of dollars [A].

Initially [1], masks used in 70° and 90° beam-deflection, delta-type tubes (tubes with masks having round apertures and dot screens) were etched so that the width of the steel strip was parallel to the observer. This is termed vertical etching. With the advent of precision in-line tubes (tubes having slit-type apertures and line screens), masks are etched so that the width of the strip is perpendicular to the observer. This horizontal etching process is necessary to prevent distortion of the slit, which occurs in vertical etching at the lower portions of the mask because ferric chloride etchant is trapped in the resist overhang. This entrapment does not occur with horizontal etching because the etchant is flushed through the aperture. As improvements have led to increased electron-beam deflection, from 70° to 110° tubes, the aperture geometry, formability of the metal, warpage, and magnetic coercivity of the mask material have all become more critical [A].

Acidified ferric chloride is widely used in industry to etch metals into burr-free precision parts, and it is one of several etchants used to make printed circuit boards. It is cheap and of low toxicity, and it reacts with a variety of metals and alloys. At RCA it is used to produce shadow masks for CRT devices from low-carbon steels. Although the parameters for running and maintaining the etch had been established

empirically over many years, little was known about its kinetics, and the photochemical-machining literature dealt mostly with printed and integrated circuits rather than precision piece-parts etched in ferric chloride [17]. To gain chemical insight into the mechanism and thermodynamics of the etch, the kinetics were first studied in a simplified ferric perchlorate–perchloric acid system, in which the reaction could be followed by UV spectrophotometry (Section 4.1) [2]. That study pointed to an encounter-limited reaction between ferric ions and the steel. To model the production process more closely, the work was then extended to concentrated ferric chloride acidified with hydrochloric acid (Sections 4.2–4.5) [B].

2. Mask Designs and Photofabrication

2.1 The photofabrication sequence (editor's outline)

This outline is the editor's summary of the standard process, given for context; the source papers describe only parts of it.

Shadow masks are made by double-sided photofabrication of continuous low-carbon steel strip, about 0.15 mm thick for the masks discussed here. The strip is cleaned and coated on both sides with a water-based photoresist (a dichromate-sensitized casein resist at RCA). It is then exposed in contact through a registered pair of glass photomasters ("artwork"). The gun-side master carries small images that will define the beam-limiting opening, and the screen-side master carries larger images that will be etched deeper to clear the beam. Water development removes the unexposed resist and leaves a stencil on each side, which is hardened by baking. The strip then passes horizontally through spray chambers, where heated, acidified ferric chloride is sprayed onto both faces through banks of nozzles until the gun-side and screen-side cavities meet ("breakthrough") and open to their final size. The resist is stripped, and the individual masks are separated, annealed, formed to the contour of the faceplate and blackened by oxidation. Defects in the resist stencil reproduce directly as aperture defects, and the size of each aperture is set by the artwork image size, the undercut of the resist during etching, and the amount of etching continued past breakthrough (Section 5).

2.2 Data-display tubes

Data-display tubes are made in medium-, high- and ultra-high-resolution versions and are used as the display medium for personal computers and for arcade and home games. Their shadow masks present formidable manufacturing challenges, which VCDD undertook successfully [A]. Fig. 1 and Table 1 give the critical dimensions of typical standard, medium-, high- and ultra-high-resolution dot masks as viewed from the gun side. Fig. 2 shows the illuminated screen structures obtained with medium-, high- and ultra-high-resolution masks.

Table 1. Comparison of typical critical dimensions for various delta-type masks (see Fig. 1) [A].

Dimension	Standard entertainment	Medium resolution	High resolution	Ultra-high resolution
A, mask pitch ("A" spacing) (mm)	0.70	0.40	0.30	0.20
B, mask aperture diameter (mm)	0.33	0.19	0.14	0.09

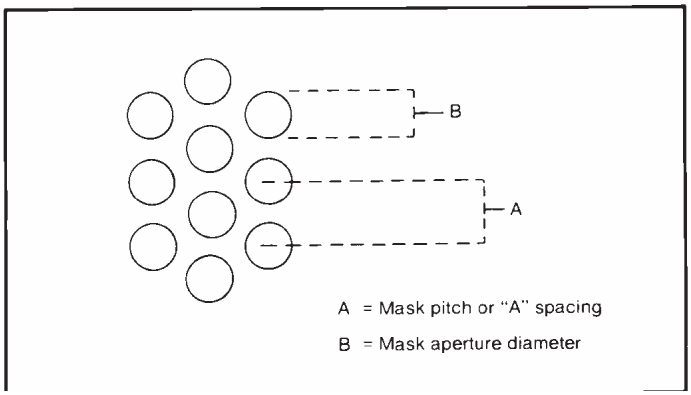


Fig. 1. Critical dimensions for delta-type masks. Both the aperture spacing and the aperture size determine the degree of resolution in data-display cathode-ray tubes [A].

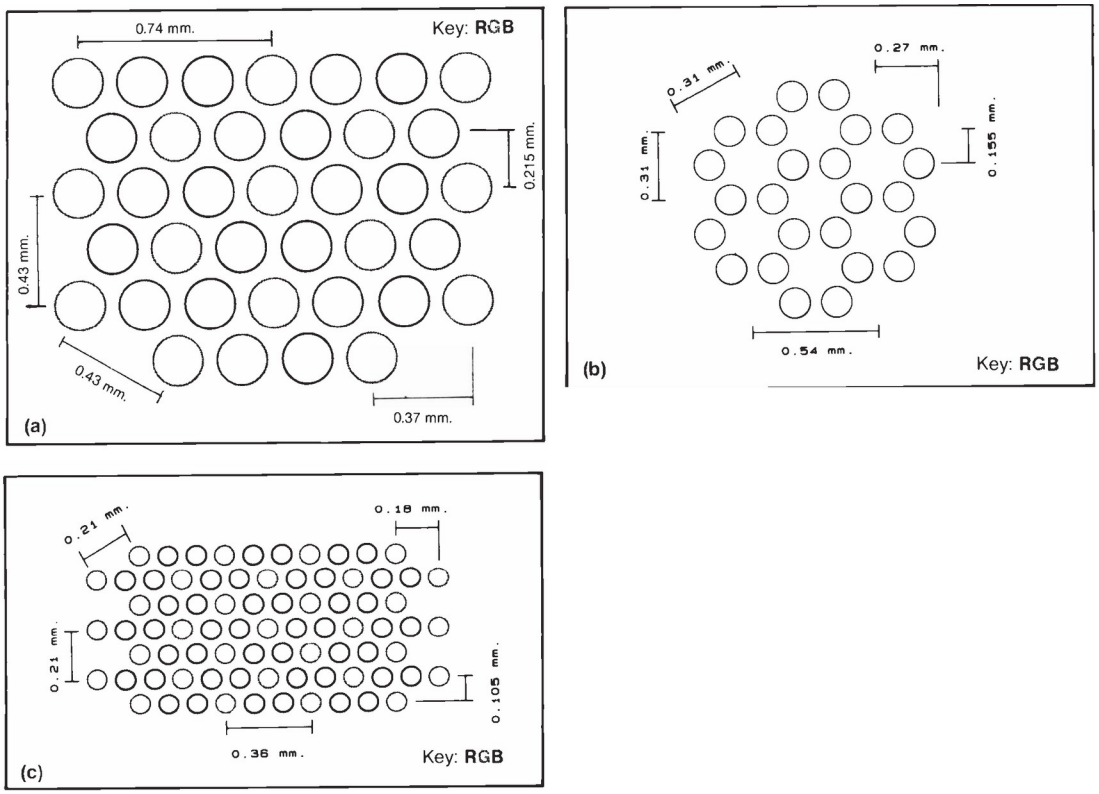


Fig. 2. Comparison of typical screen structures for display tubes: (a) typical medium-resolution screen structure, (b) typical high-resolution screen structure for RCA data displays, and (c) typical ultra-high-resolution screen structure [A].

Fig. 3 compares, from the screen side, an RCA 13V/90° COTY mask and an RCA 13V/90° high-resolution display mask. The packing density of apertures in the high-resolution mask is three times that of the conventional entertainment mask. Artwork requirements and etching yields are therefore severely tested by the increased number of apertures per unit area. The mask cannot have a single imperfection that would degrade screen quality, and its visual uniformity must be acceptable in both the flat and formed states. These were the basic manufacturing challenges VCDD faced [A].

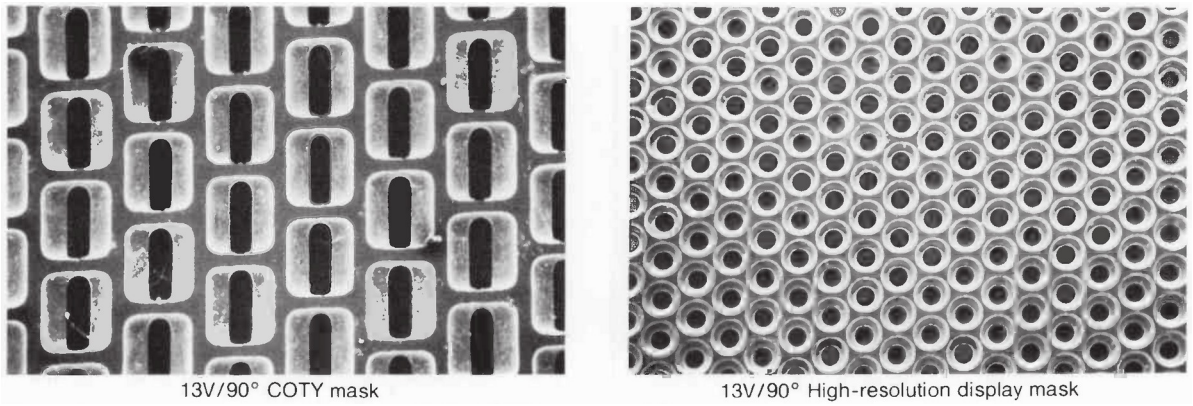


Fig. 3. Comparison of equivalent areas for 13V/90° COTY and 13V/90° high-resolution display masks. The number of high-resolution display apertures is three times the number of apertures per unit area in entertainment-type masks [A].

3. Mask Metallurgy

In the early phases of etching high-resolution data-display masks at RCA, conventional rimmed steel (0.10% carbon, cold-rolled) gave masks with poor uniformity, which degraded further after annealing and forming. A significant improvement in flat and formed mask uniformity was achieved when aluminum-killed (AK) cold-rolled steel was used in place of rimmed steel. Fig. 4 shows flat-mask apertures made from rimmed and from aluminum-killed steel. The aperture edge in the AK steel is clearly superior, and the ragged apertures in rimmed steel partly account for its poor mask uniformity [A].

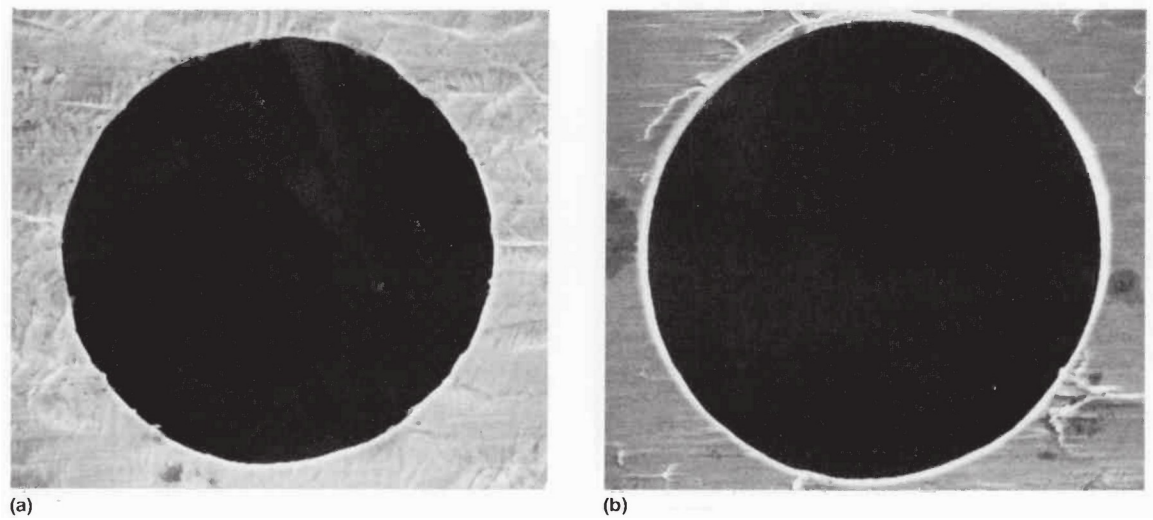


Fig. 4. Comparison of rimmed-steel and aluminum-killed-steel display-mask apertures: (a) rimmed-steel display aperture, and (b) aluminum-killed-steel display aperture. The rimmed-steel apertures have ragged edges. This condition is not present in aluminum-killed steel, which gives better visual uniformity in the finished mask [A].

The chemical compositions of rimmed and AK steels are compared in Table 2. The impurity levels in AK steel are somewhat lower than in rimmed steel, and they are uniformly distributed throughout the material. Rimmed steel has a higher carbon content (0.10%) and an anisotropic distribution of all the impurities, which gives uneven etching and nonuniform stretching of the metal [A].

Table 2. Typical chemical composition (weight percent) of rimmed and aluminum-killed steels. Single values are maximum allowed; n.d. = not detectable [A].

Steel	C	Si	Mn	P	S	Cr	Cu	Al	Fe
Rimmed	0.10	0.10	0.25–0.50	0.040	0.050	n.d.	n.d.	n.d.	balance
Aluminum-killed	0.006	0.05	0.25–0.50	0.020	0.020	0.05	0.08	0.02–0.08	balance

Nonuniform stretching during mask forming can also come from a metallurgical property termed yield-point elongation (YPE). Fig. 5 shows tensile curves for materials with and without YPE. AK steel can easily be annealed to remove YPE, another reason for selecting it for data-display shadow masks [A].

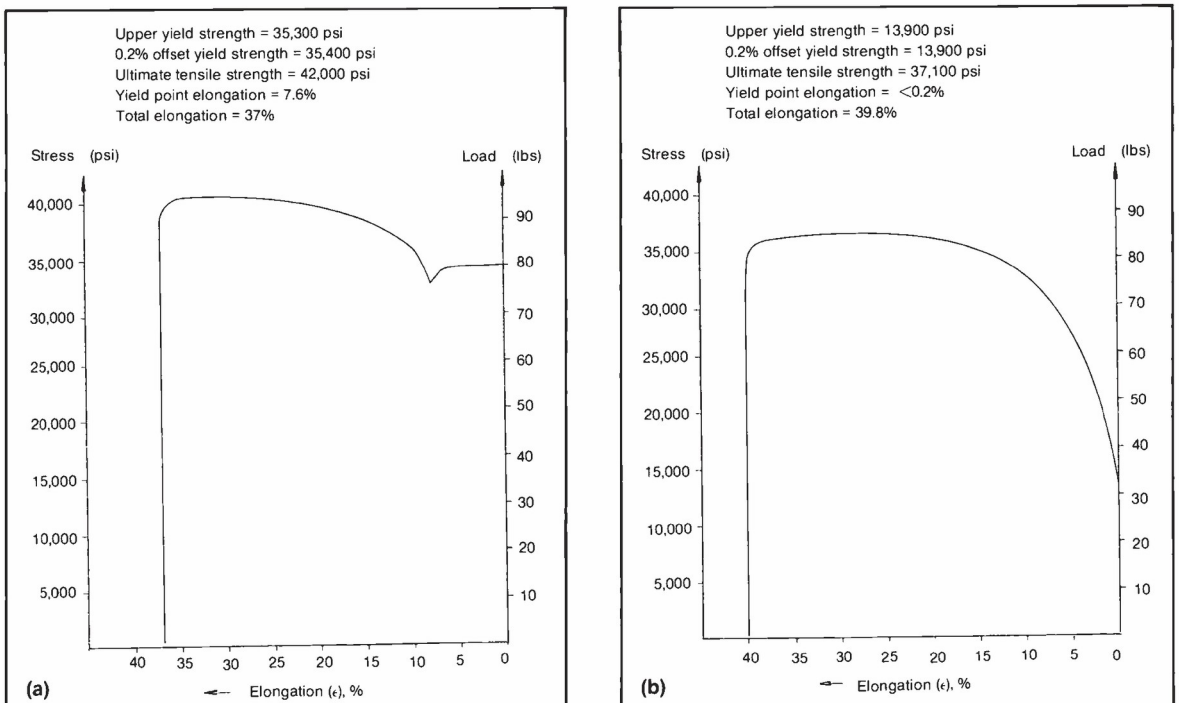


Fig. 5. Stress against elongation (after annealing) for (a) rimmed and (b) aluminum-killed steel. The rimmed material shows a discontinuous feature, yield-point elongation (YPE), that is not present in the aluminum-killed steel; YPE is a source of nonuniformity in the formed and blackened mask. (a) Upper yield strength 35 300 psi [243 MPa], 0.2% offset yield strength 35 400 psi [244 MPa], ultimate tensile strength 42 000 psi [290 MPa], YPE 7.6%, total elongation 37%. (b) Upper and 0.2% offset yield strength 13 900 psi [95.8 MPa], ultimate tensile strength 37 100 psi [256 MPa], YPE < 0.2%, total elongation 39.8% [A].

Rimmed and AK steels etch at the same rate in ferric chloride (Section 4.4) and in ferric perchlorate (Section 4.1). The benefit of AK steel therefore comes from its more uniform microstructure and better forming behavior, not from any difference in etch rate.

4. Etch Chemistry and Kinetics

4.1 Model system: ferric perchlorate–perchloric acid

Concentrated ferric chloride contains several ferric chloro complexes in equilibrium (Section 4.5), which makes the chemistry hard to untangle. The kinetics were therefore studied first in perchlorate solution, where perchlorate does not coordinate to iron, so only one ferric species, the hexaaquo ion, is present and its loss can be followed spectrophotometrically [C].

Experimental. Ferric and ferrous perchlorates (Alfa) and all other chemicals (GFS Chemicals) were reagent grade and used as received, with deionized water throughout. Rectangular pieces of 1008 rimmed steel, 36 × 55 × 0.15 mm, were cleaned in hot caustic, rinsed and dried. Observed rate constants varied by as much as about 15% between steel from different coils, mainly because of differences in surface microstructure from the previous cold working and heat treatment, an effect also known in corrosion [23]. Pieces from the same coil were therefore used whenever a particular parameter was varied. The orientation of the steel had no effect [C].

The reaction vessel was the tall one-liter beaker assembly described in Section 4.2, with an extra sampling port in the cover, held at ±0.05 °C. A typical solution was 0.75 M in perchloric acid and 5.0×10^{-3} M in ferric perchlorate, with lithium perchlorate added to an ionic strength of 1.0. A 500-mL portion was brought to temperature while stirred with a Mylar strip, which was then replaced by the steel piece. 1.00-mL samples were withdrawn every ten minutes (15 samples over 140 minutes) and analyzed for ferric hexaaquo ion at 240 nm; less than 4% of the solution was removed in all. Each solution was stirred at 75 rpm until the 70-minute sample and then at 125 rpm, and the second 500-mL portion was run with the order reversed. Acid-concentration and ionic-strength runs used 100 rpm for 100 minutes. Vortexing began above 175 rpm, which was the highest speed used. Pseudo-first-order rate constants were obtained by linear regression of $\ln([Fe^{3+}]_0/[Fe^{3+}]_t)$ against time, and averages were taken over at least three runs [C].

Rate law. The rate of disappearance of the ferric hexaaquo ion, $Fe(H_2O)_6^{3+}$ (written Fe^{3+}), depends on its concentration, $c = [Fe^{3+}]$, and on the physical characteristics of the steel surface:

$$-\frac{dc}{dt} = k_h c^a f(Fe) \quad (1)$$

where f(Fe) contains all the surface characteristics that influence the rate, k_h is the heterogeneous rate constant and a is the reaction order in ferric ion. The steel was always in large excess, so the reaction is pseudo-zero-order in iron:

$$-\frac{dc}{dt} = k_{obs} c^a \quad (2)$$

For a = 1, integration gives

$$\ln c_t = \ln c_0 - k_{obs} t \quad (3)$$

so a plot of $\ln([Fe^{3+}]_0/[Fe^{3+}]_t)$ against time is a straight line of slope k_{obs} [C].

Order in ferric ion. Fig. 6 shows ferric ion concentration against time for a run starting at 7.47×10^{-3} M, sampled every 20 minutes for 400 minutes at 75 rpm, and Fig. 7 shows the same data plotted according to Equation 3. The line is straight over at least 3½ half-lives (more than 90% of the ferric ion consumed), so the reaction is first order in ferric hexaaquo ion. Table 3 confirms that k_{obs} is nearly

constant for initial concentrations from 1.0×10^{-3} to 9.6×10^{-3} M. Fig. 8 illustrates the internal consistency of the protocol: the two halves of each pair of runs, with the two stirring speeds taken in opposite order, meet at or near the 140-minute point, as they should [C].

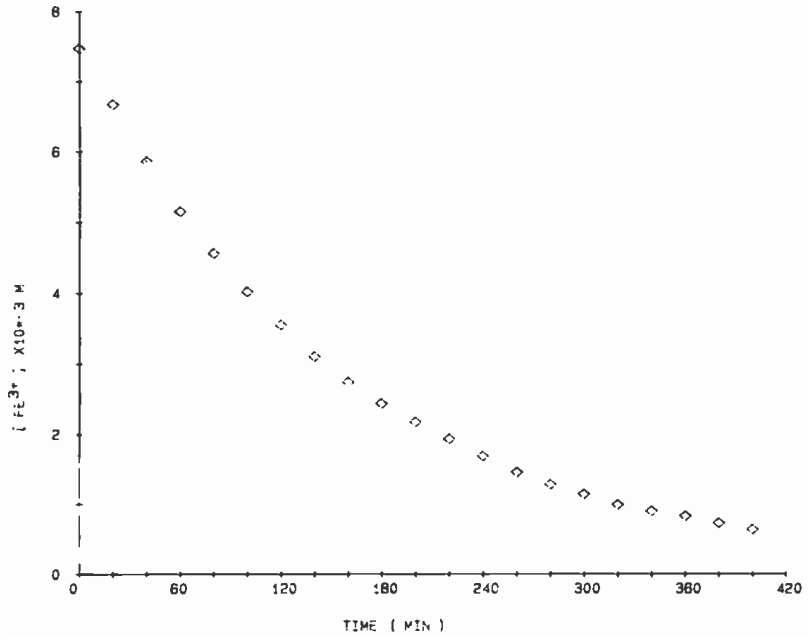


Fig. 6. Ferric hexaaquo ion concentration (10^{-3} M) against reaction time for an initial concentration of 7.47×10^{-3} M at 29.8 °C and 75 rpm [C].

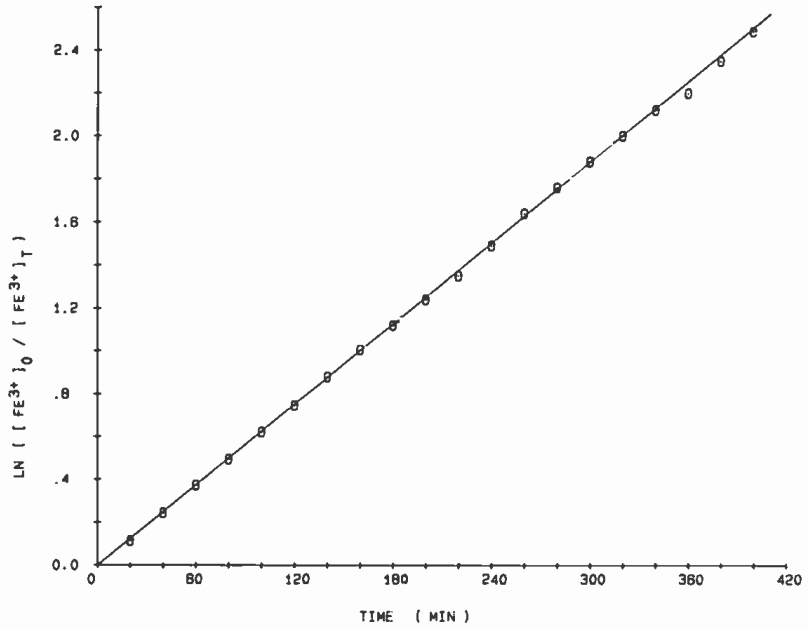


Fig. 7. $\ln([Fe^{3+}]_0/[Fe^{3+}]_t)$ against reaction time for the data of Fig. 6 [C].

Table 3. Average observed rate constants at 29.8 °C [C].

Initial $[Fe^{3+}]$ (M)	Stirring speed (rpm)	k_{obs} (10^{-3} min^{-1})
9.61×10^{-3}	75	6.46 ± 0.11

Initial [Fe^{3+}] (M)	Stirring speed (rpm)	k_{obs} (10^{-3} min^{-1})
	125	8.80 ± 0.06
4.50×10^{-3}	75	6.30 ± 0.12
	125	8.61 ± 0.06
1.0×10^{-3}	75	6.0 ± 0.1
	125	8.0 ± 0.1

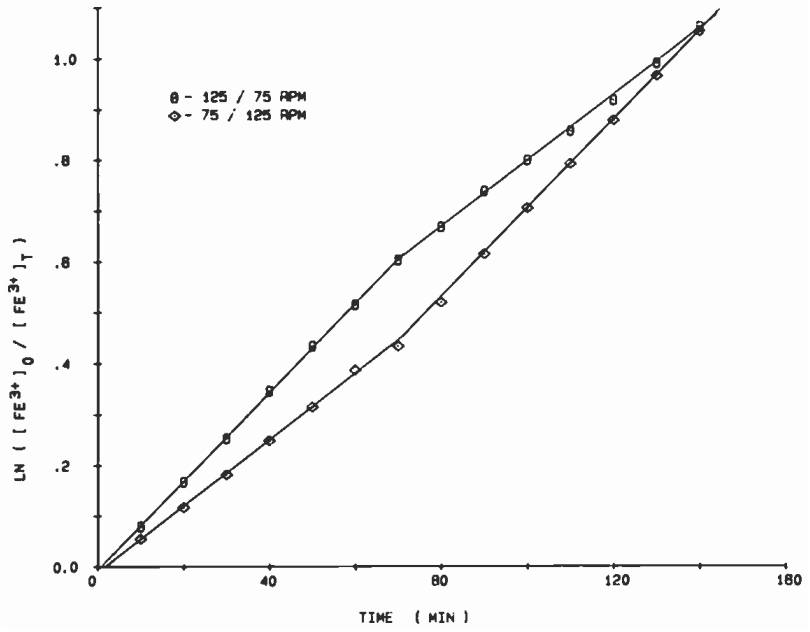


Fig. 8. A representative pair of runs illustrating the consistency of the kinetic data: one portion stirred at 75 then 125 rpm, the other at 125 then 75 rpm [C].

Stirring. The rate constant increases with stirring speed (Fig. 9), as expected for encounter-limited kinetics: better agitation thins the boundary layer and speeds the arrival of ferric ions at the metal. (The "rate of encounter" combines mass transport of bulk solution to the interface and diffusion across it to the steel; the two were not separated.) The data from 75 to 175 rpm fall almost exactly on a straight line. Below 75 rpm they fall below it, apparently because the bulk solution is stirred inefficiently; even with no stirring the reaction would proceed at a finite rate by pure diffusion [C].

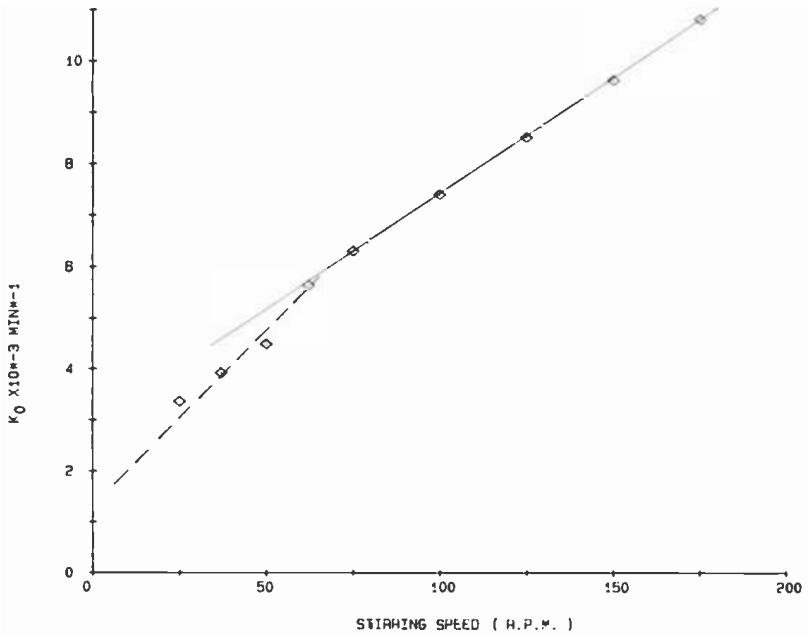


Fig. 9. Dependence of the observed rate constant (10^{-3} min^{-1}) on stirring speed at 29.8 °C [C].

Ferrous ion, acid and ionic strength. Initial ferrous ion from 2.5×10^{-3} to 2.0×10^{-2} M had no systematic effect on k_{obs} (Table 4). Regression on the four ferrous concentrations gives intercepts of 6.26 $\times 10^{-3}$ and 8.47 $\times 10^{-3}$ min^{-1} at 75 and 125 rpm, close to the values with no ferrous ion. Ferrous ion is nevertheless involved in the surface chemistry in some way: higher initial ferrous concentrations, especially 0.010 M and above, formed a heavier dark coating on the steel, yet without any noticeable inhibition [C].

Table 4. Average observed rate constant as a function of initial ferrous concentration at 29.8 °C [C].

Initial $[Fe^{2+}]$ (M)	Stirring speed (rpm)	k_{obs} (10^{-3} min^{-1})
0	75	6.30 ± 0.10
	125	8.51 ± 0.10
0.0025	75	6.10 ± 0.35
	125	8.32 ± 0.10
0.0050	75	6.46 ± 0.26
	125	8.39 ± 0.10
0.010	75	6.10 ± 0.11
	125	8.63 ± 0.33
0.020	75	6.15 ± 0.34
	125	8.17 ± 0.08

The rate constant was independent of perchloric acid concentration from 0.05 to 0.90 N, consistent with ferric hydrolysis being kept to a minimum (about 1–2% of the ferric content was hydrolyzed at 0.05 N). Between 0.01 and 0.05 N the runs were not reproducible. Those solutions, clear on mixing, turned yellow

from ferric hydrolysis within a short time at 29.8 °C, and solutions left for several hours would not etch the steel even though most of the iron was still present as ferric hexaaquo ion. Raising the ionic strength from 1.0 to 3.0 with either lithium or sodium perchlorate lowered k_{obs} nonlinearly (Table 5). The likely cause is a change in the activity coefficient of the ferric ion, through ion association [18], lower ionic mobility [19] or higher viscosity [20] [C].

Table 5. Average observed rate constant against ionic strength at 29.8 °C and 100 rpm [C].

Ionic strength	k_{obs}, $NaClO_4$ (10^{-3} min^{-1})	k_{obs}, $LiClO_4$ (10^{-3} min^{-1})
1.0	6.35 ± 0.05	6.44 ± 0.10
2.0	6.25 ± 0.37	6.16 ± 0.05
3.0	5.46 ± 0.12	5.47 ± 0.06

Viscosity, volume and area. Over the limited range of viscosities available, log–log regression gives $k_{obs} \propto \eta^{-1.34\pm0.33}$ at 75 rpm and $\eta^{-1.00\pm0.38}$ at 125 rpm, a roughly inverse dependence on viscosity (Fig. 10). Increasing the solution volume lowers k_{obs}, with exponents of −0.74 ± 0.07 and −0.76 ± 0.03 (Fig. 11; see Editor's Note 6). Doubling the steel area doubles k_{obs}, with exponents of 1.03 ± 0.09 and 1.02 ± 0.11 (Fig. 12). AK and FS steels gave the same rate constants as 1008 rimmed steel [C].

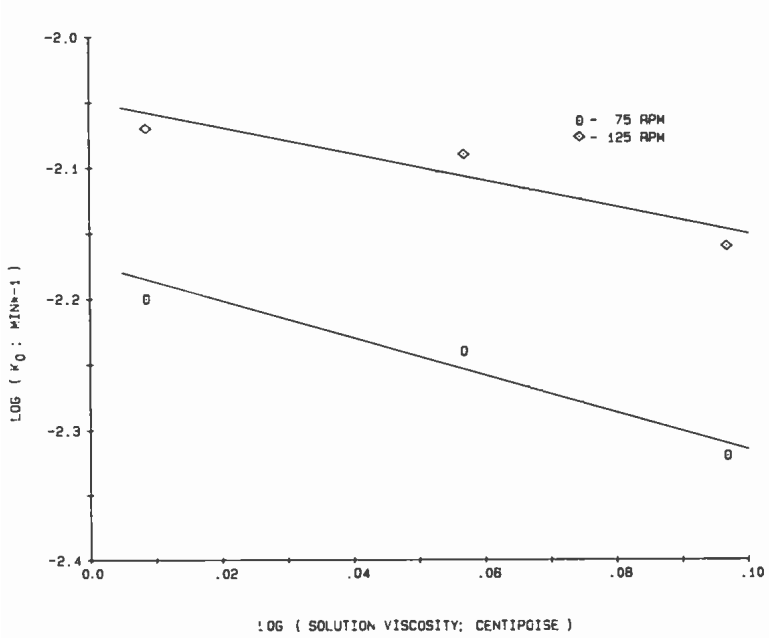


Fig. 10. Log–log plot of observed rate constant (min^{-1}) against solution viscosity (cP) at 29.8 °C, at 75 and 125 rpm [C].

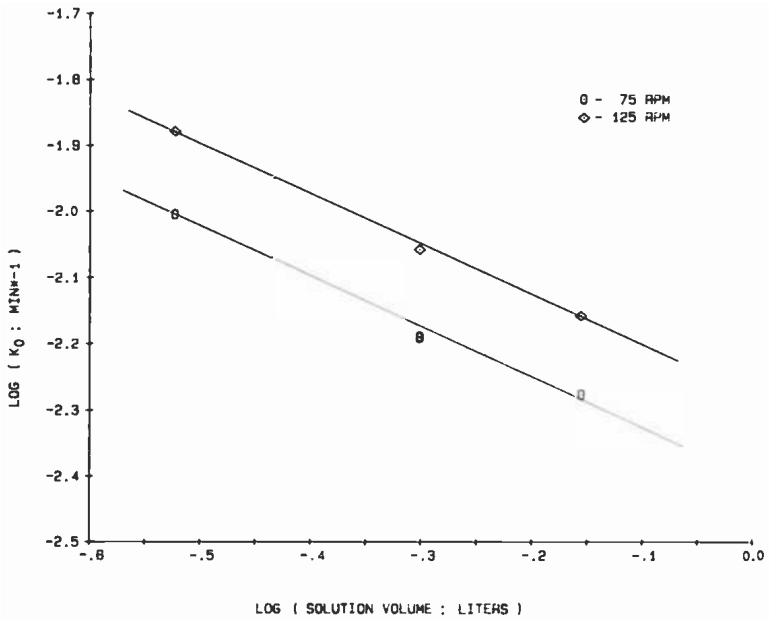


Fig. 11. Log–log plot of observed rate constant (min^{-1}) against solution volume (L) at 29.8 °C [C].

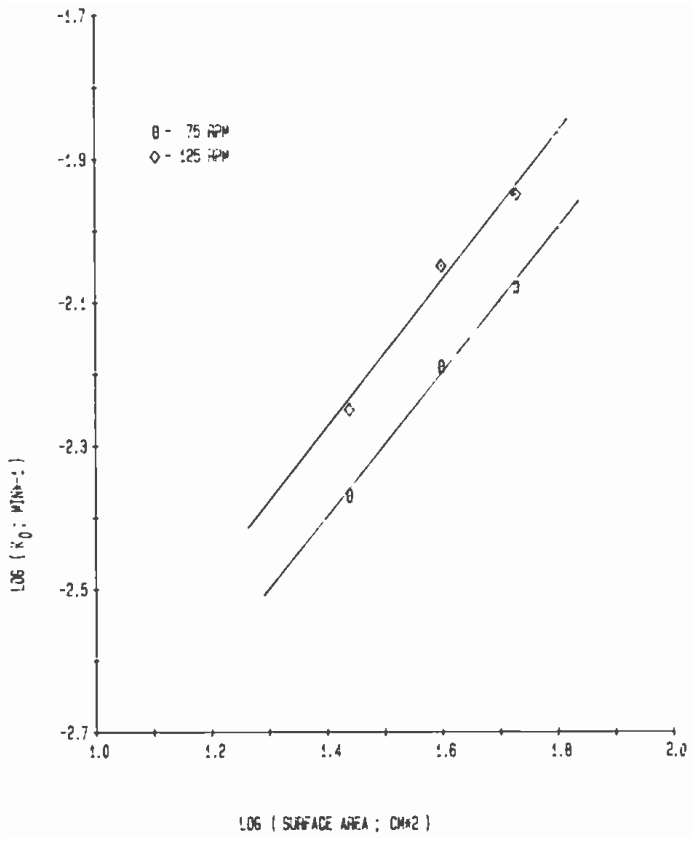


Fig. 12. Log–log plot of observed rate constant (min^{-1}) against area of the steel piece (cm^2) at 29.8 °C [C].

Temperature. Table 6 gives k_{obs} from 29.8 to 50.1 °C. At 40.2 and 50.1 °C, hydrogen evolution produced bubbles on the steel. Tapping the stirring rod minimized partial blocking of the surface, and a series at 50.1 °C with the perchloric acid lowered from 0.75 to 0.050 N, which reduces hydrogen evolution, gave virtually identical rate constants. Arrhenius and Eyring plots (Figs. 13 and 14; Equations 4 and 5 of

Section 4.3) give the activation parameters of Table 7. The two stirring speeds agree within 2σ, and average to $E_a \approx 3.5$ kcal/mol [15 kJ/mol], $\Delta H^{\ddagger} \approx 2.8$ kcal/mol [12 kJ/mol] and $\Delta S^{\ddagger} \approx -20$ eu [C].

Table 6. Average observed rate constant as a function of temperature at ionic strength 1.0 [C].

T (K)	k_{obs} at 75 rpm (10^{-4} s^{-1})	k_{obs} at 125 rpm (10^{-4} s^{-1})
303.0 (29.8 °C)	0.860 ± 0.010	1.10 ± 0.02
313.4 (40.2 °C)	1.07 ± 0.02	1.38 ± 0.02
323.3 (50.1 °C)	1.25 ± 0.06	1.56 ± 0.02
323.3 (50.1 °C), $HClO_4$ 0.050 N	1.25 ± 0.02	1.54 ± 0.04

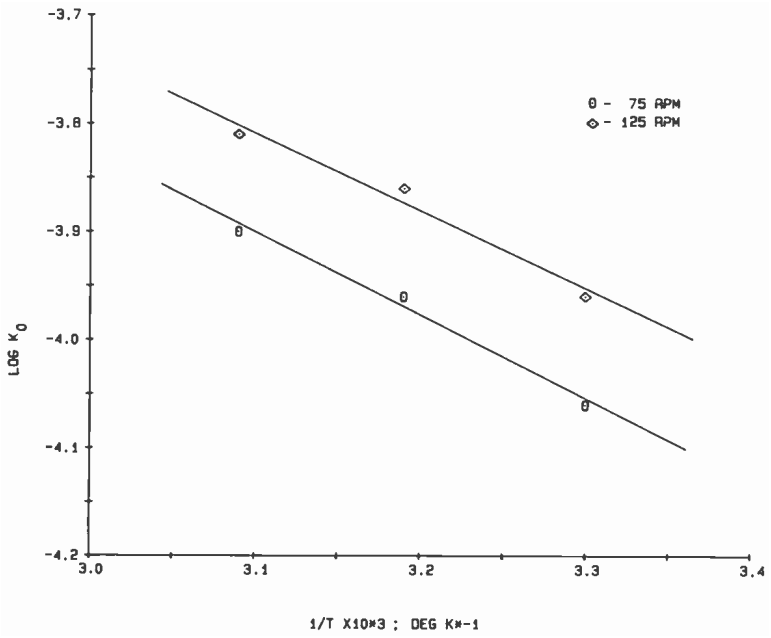


Fig. 13. Arrhenius plot of log k_{obs} (s^{-1}) against 1/T for the ferric perchlorate system at 75 and 125 rpm [C].

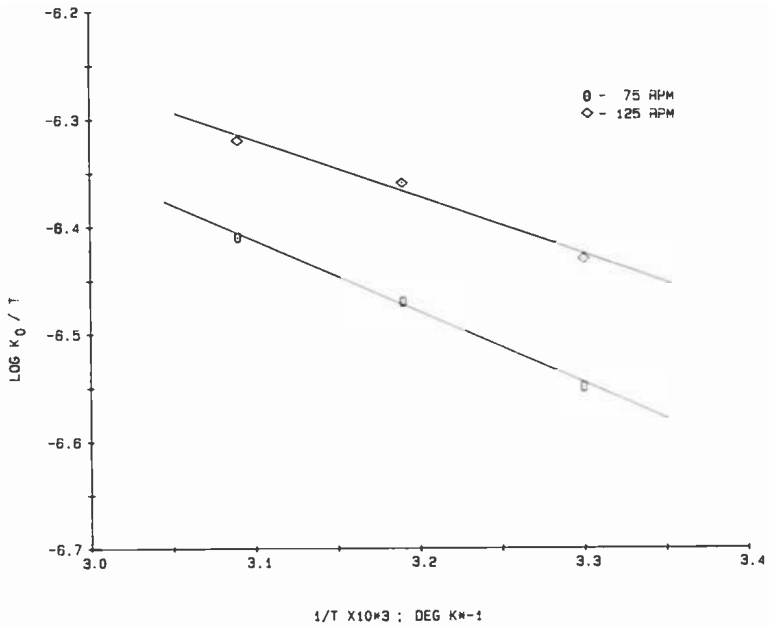


Fig. 14. Eyring plot of log(k_{obs}/T) against 1/T for the ferric perchlorate system at 75 and 125 rpm [C].

Table 7. Activation parameters for the ferric perchlorate system [C]. For ΔS‡ see Editor's Note 3.

Stirring speed (rpm)	E_a (kcal/mol) [kJ/mol]	ΔH‡ (kcal/mol) [kJ/mol]	ΔS‡ (eu) [J mol^{-1} K^{-1}]
75	3.71 ± 0.27 [15.5]	3.06 ± 0.16 [12.8]	−19.8 ± 0.5 [−83]
125	3.28 ± 0.51 [13.7]	2.63 ± 0.43 [11.0]	−20.8 ± 1.4 [−87]

Mechanism. The results show the qualitative signs of an encounter-limited reaction. The rate depends on stirring speed and steel area and inversely on solution volume; it varies roughly inversely with viscosity; and the enthalpy of activation is low, within the 1–4 kcal/mol range typical of diffusion of small molecules in solvents of low viscosity [6]. (A rigorous proof would need an exact analysis of mass transfer to the steel as a function of agitation and viscosity, which the geometry of the samples does not allow [22].) As for the chemistry, the reaction is first order in ferric hexaaquo ion, it is neither inhibited nor catalyzed by excess ferrous ion, minor metals in the different steels neither catalyze nor inhibit it, and it is independent of acid from 0.050 to 0.90 N. A plausible mechanism is [C]:

$Fe(H_2O)_6^{3+} + Fe(H_2O)_n(s) \rightarrow Fe(H_2O)_n{\cdot}Fe(H_2O)_6^{3+}$ (slow) (6)

$Fe(H_2O)_n{\cdot}Fe(H_2O)_6^{3+} \rightarrow Fe(H_2O)_n^{+}(ads) + Fe(H_2O)_6^{2+}$ (fast) (7)

$Fe(H_2O)_n^{+}(ads) + Fe(H_2O)_6^{3+} \rightarrow 2\ Fe(H_2O)_6^{2+}$ (fast) (8)

The rate-determining step (6) is the encounter of a ferric hexaaquo ion with the hydrated steel surface, which includes the mass transport and diffusion that bring it there from the bulk solution. The negative entropy of activation is consistent with this step. It is followed by adsorption and fast electron transfer, forming a reactive monovalent iron species that rapidly reduces a second ferric ion. The steps after the rate-determining one are conjecture, but they are plausible. First, an adsorbed Fe(I) intermediate has been implicated in several corrosion studies [21], and a soluble Fe(I) species is unlikely given its reactivity. Second, the stoichiometry, $Fe + 2Fe^{3+} \rightarrow 3Fe^{2+}$, requires two ferric ions per iron atom, so with a first-order rate law the second must react in a fast step after the rate-limiting one. Third, since added

ferrous ion does not inhibit the reaction, desorption of ferrous products must be faster than adsorption. On this mechanism, the faster ferric ions are carried to the steel, the faster the etch, at least until transport and adsorption become comparable with desorption and removal of products. The model system greatly simplifies the production process, but it gives insight into the dynamics of etching. Sections 4.2–4.5 extend the study to concentrated ferric chloride [C].

4.2 Ferric chloride: experimental

Rectangular pieces of various steels measuring 36 × 52 mm were used. All were 0.15 mm thick except the FS steel, which was 0.10 mm thick. All were cleaned by soaking in hot caustic solution, thoroughly rinsed with deionized water, and dried. Ferric chloride concentration was obtained by measuring etchant density with hydrometers calibrated on the heavy Baumé scale; specific gravity and molar concentration of ferric chloride can be interpolated from standard tables [B].

Stock solutions of ferric chloride etchant were analyzed for ferrous chloride, ferric chloride and free acid. Higher Baumés were obtained by boiling water off the stock etchant, and lower Baumés by dilution with hydrochloric acid and deionized water. Except where noted, the free-acid concentration was adjusted to 0.040 M [B].

Viscosity was measured with a Brookfield LVF viscometer fitted with a modified ultra-low-viscosity adapter (a titanium insert of 2.4 cm internal diameter and a Teflon #1 LV spindle), calibrated with a Brookfield viscosity standard. All measurements were taken at 60 rpm on a scale covering 0–50.5 centipoise [0–50.5 mPa·s] [B].

The reaction vessel was a tall one-liter beaker in a Plexiglas–CPVC assembly with a grooved Plexiglas cover drilled for a thermometer and a Teflon stirring rod. A piece of steel was held in a slot in the stirring rod, which was driven by a variable-speed motor. The assembly was placed in a constant-temperature water bath controlled to ±0.05 °C. In a typical experiment, 0.5 L of etchant was brought to temperature while being stirred with a strip of Mylar, which was then replaced by a preweighed piece of steel. Depending on temperature and Baumé, the steel was etched until about 0.1–0.4 g had been removed, generally in 2–6 minutes. It was then immediately rinsed with deionized water, dried and weighed. At least three pieces were etched at each temperature and Baumé from the same etchant sample. Stirring speed was held to ±1 rpm, monitored with a digital phototachometer; except where noted, all experiments used 100 rpm. Surface roughness was measured with a Bendix Type QC profilometer, and Baumé with hydrometers calibrated to 0.1° [B].

Etch rates (g cm^{-2} s^{-1}) were calculated from the weight removed per apparent surface area and reaction time. Heterogeneous rates (cm s^{-1}) were obtained by dividing etch rates by the density of the steel (7.87 g cm^{-3}) [B].

4.3 Ferric chloride: etch rate, surface finish and activation parameters

Fig. 15 shows the average etch rates for beaker etching 1008 rimmed steel at five temperatures from 40 to 80 °C (104–176 °F) and Baumés from 30° to 58°. Standard deviations are generally 1–4% of the reported values for 40–70 °C. At 80 °C many standard deviations exceeded 10% because of experimental difficulties at this temperature, so the 80 °C curve shows more scatter. Eccentricities of several millimeters in the stirring rod had no discernible effect. Pieces etched under identical conditions for different times (1–5 minutes) had nearly identical etch rates, and the rate did not depend on the order in which samples were etched [B].

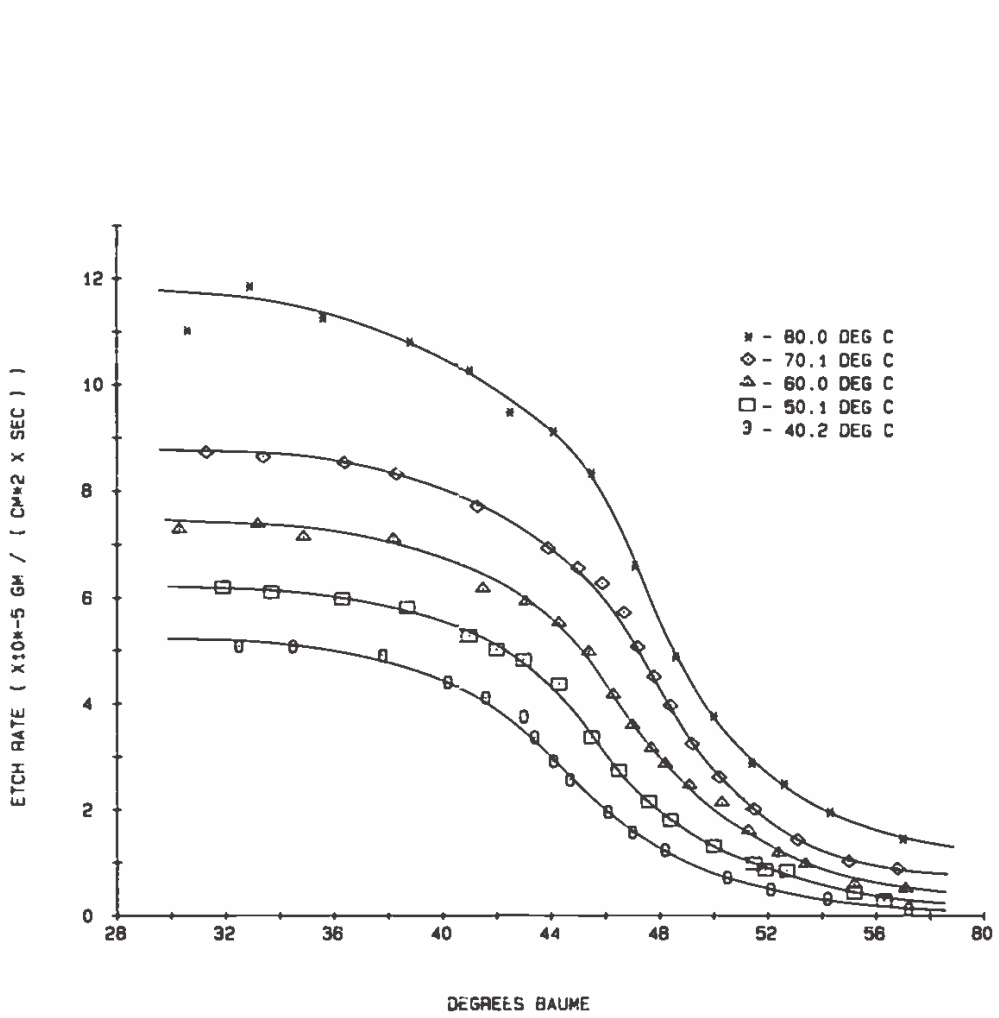


Fig. 15. Average etch rates (10^{-5} g cm^{-2} s^{-1}) for 1008 rimmed steel as a function of Baumé and temperature (40.2, 50.1, 60.0, 70.1 and 80.0 °C) [B]. An etch rate of 5×10^{-5} g cm^{-2} s^{-1} corresponds to about 3.8 µm per minute from each face.

A representative sample from each kinetic experiment was measured for surface roughness (Fig. 16). At each temperature there is a sharply defined transition from smooth (below 10 microinches [0.25 µm]) to rough (above 10 microinches) finish as the Baumé is lowered. The transition Baumé is temperature dependent, increasing by about one degree Baumé for every 10 °C up to 70 °C, with only a slight further increase from 70 to 80 °C. The increase in roughness coincides with the appearance of smut on the steel surface; its nonuniform coverage probably contributes to the rough finish. The roughness also appears to increase with temperature [B].

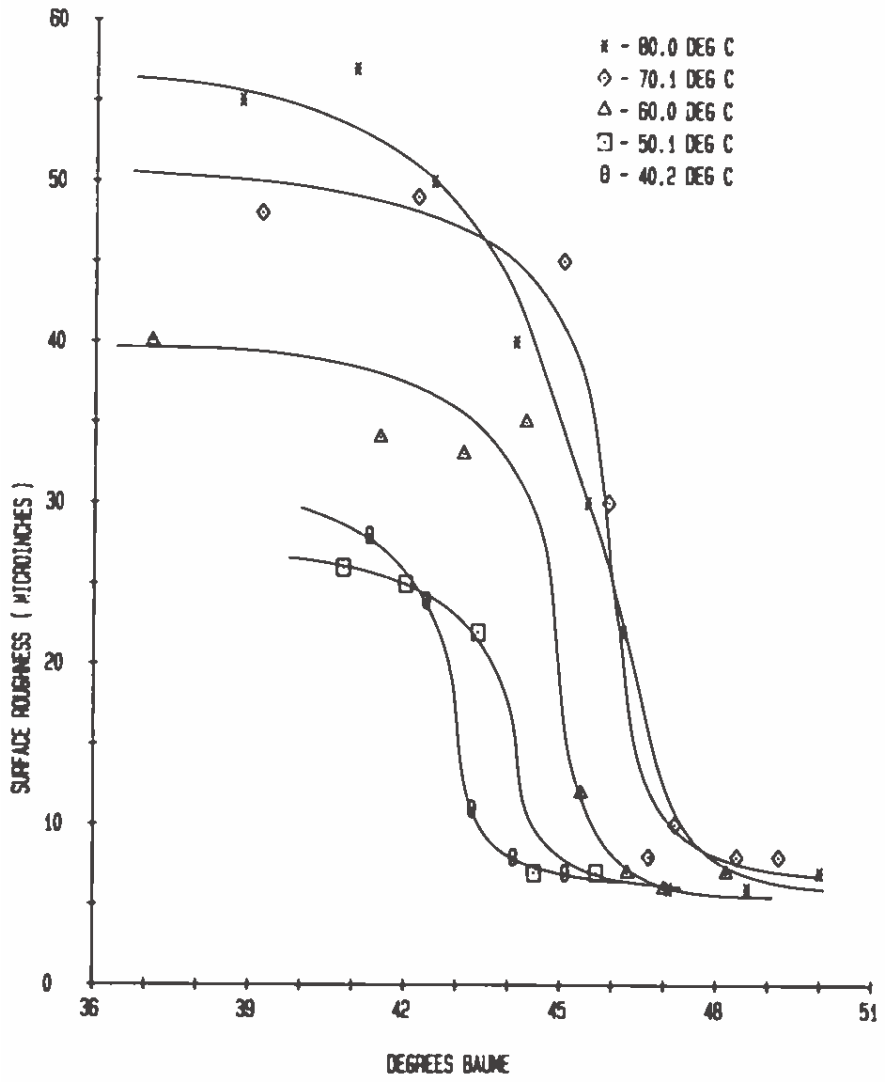


Fig. 16. Average surface roughness (microinches; 1 µin = 0.0254 µm) for 1008 rimmed steel as a function of Baumé and temperature [B].

Activation parameters were obtained from heterogeneous rate constants. A best-fit curve was hand-fitted to each set of data from 40.2 to 70.1 °C in Fig. 15 (the 80.0 °C data were excluded because of their scatter), rate constants at 32.0° and 57.0° Bé were read from the curves, and each was divided by the density of 1008 rimmed steel (7.87 g cm^{-3}) to give Table 8 [B].

Table 8. Observed heterogeneous rate constants as a function of temperature for 1008 rimmed steel at a stirring rate of 100 rpm [B]. (The 32.0° Bé column is printed as 10^{-8} cm s^{-1} in the original; see Editor's Note 2.)

T (K)	k at 32.0° Bé (10^{-6} cm s^{-1})	k at 57.0° Bé (10^{-7} cm s^{-1})
313.4 (40.2 °C)	6.54	2.06
323.3 (50.1 °C)	7.85	3.94
333.2 (60.0 °C)	9.34	6.49
343.3 (70.1 °C)	11.0	10.5

The effect of absolute temperature T on the heterogeneous rate constant k is described by the Arrhenius relation

$$k = A \exp\left(-\frac{E_a}{RT}\right) \quad (4)$$

where E_a is the activation energy and A the pre-exponential factor, which is related to entropy [4]. A plot of log k against 1/T is linear with slope $-E_a/2.303R$. Alternatively, the free energy, enthalpy and entropy of activation follow from the Eyring relation

$$k = \frac{k_B T}{h} \exp\left(-\frac{\Delta G^{\ddagger}}{RT}\right) = \frac{k_B T}{h} \exp\left(-\frac{\Delta H^{\ddagger}}{RT}\right) \exp\left(\frac{\Delta S^{\ddagger}}{R}\right) \quad (5)$$

where k_B is Boltzmann's constant and h Planck's constant [5]. A plot of log(k/T) against 1/T is linear with slope $-\Delta H^{\ddagger}/2.303R$. Arrhenius and Eyring plots are shown in Figs. 17 and 18, and the activation parameters are collected in Table 9 [B].

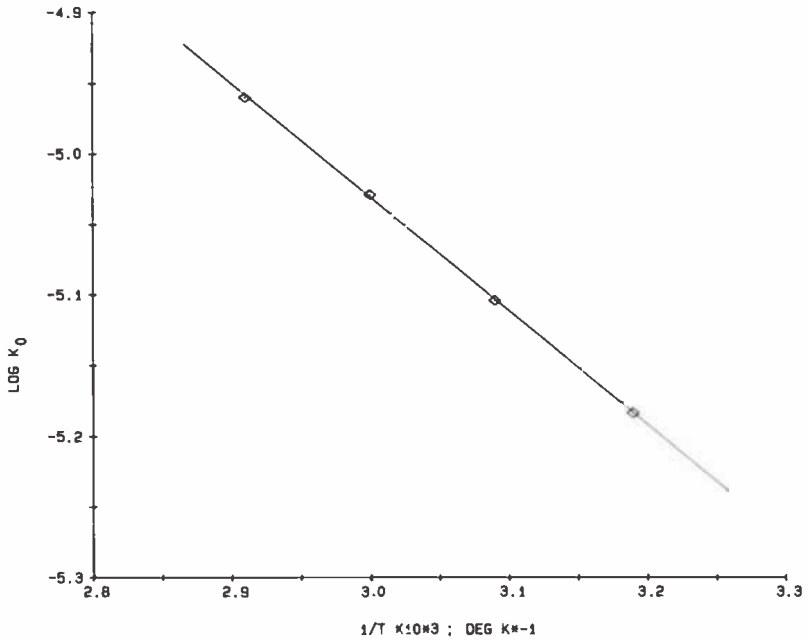


Fig. 17. Arrhenius plot of log k against 1/T at 32.0° Baumé for 1008 rimmed steel [B].

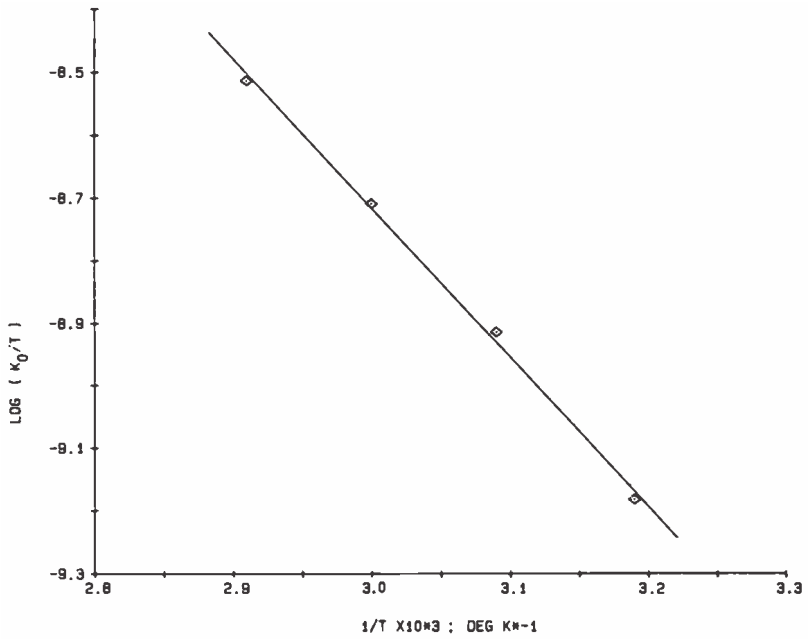


Fig. 18. Eyring plot of log (k/T) against 1/T at 57.0° Baumé for 1008 rimmed steel [B].

Table 9. Activation parameters [B]. For the ΔS‡ values see Editor's Note 3.

Baumé	E_a (kcal/mol) [kJ/mol]	ΔH‡ (kcal/mol) [kJ/mol]	ΔS‡ (eu) [J mol^{-1} K^{-1}]
32.0°	+3.69 ± 0.12 [15.4]	+3.07 ± 0.13 [12.8]	−25.3 ± 0.3 [−106]
57.0°	+11.5 ± 0.5 [48.1]	+10.9 ± 0.5 [45.6]	−7.2 ± 1.2 [−30]

4.4 Ferric chloride: effect of chloride, steel type and viscosity

The effect of added chloride ion, as either hydrochloric acid or lithium chloride, is shown in Table 10 for low, medium and high Baumé, compared with the etch rate at the same Baumé on the standard curves of Fig. 15 [B].

Table 10. Etch rates for 1008 rimmed steel at 50.1 °C and 100 rpm (initial free-acid concentration 0.010 M) [B].

Region	Added HCl (M)	Added LiCl (M)	Baumé	Etch rate (10^{-5} g cm^{-2} s^{-1})	Change from standard curve (%)
Low	0.23		40.7	5.27 ± 0.13	−1.3
		0.23	40.8	5.21 ± 0.14	−1.9
	0.46		39.9	5.41 ± 0.13	−2.2
		0.46	40.0	5.25 ± 0.10	−4.7
Medium	0.012		47.3	2.34 ± 0.02	+1.3
		0.012	47.4	2.29 ± 0.06	+1.5

Region	Added HCl (M)	Added LiCl (M)	Baumé	Etch rate (10^{-5} g cm^{-2} s^{-1})	Change from standard curve (%)
	0.058		47.5	2.28 ± 0.04	+3.6
		0.058	47.5	2.25 ± 0.01	+2.3
	0.23		47.4	2.20 ± 0.01	−2.6
		0.23	47.6	2.13 ± 0.04	−0.9
	0.46		46.4	2.48 ± 0.02	−11.1
		0.46	46.5	2.45 ± 0.02	−10.6
High	0.053		53.7	0.688 ± 0.006	+1.3
		0.053	53.3	0.764 ± 0.017	+2.7
	0.11		53.7	0.621 ± 0.004	−8.5
		0.11	54.0	0.568 ± 0.007	−9.8
	0.21		54.5	0.484 ± 0.012	−14.4
		0.21	54.4	0.461 ± 0.008	−18.4

Two trends are evident. First, the etch rate at a given Baumé depends on the added chloride concentration irrespective of whether it is added as hydrochloric acid or lithium chloride. Etch-rate depression is therefore not a function of free-acid concentration; the only role of free acid appears to be to keep the pH low enough to prevent ferric hydrolysis and precipitation of iron hydroxides. Second, as the Baumé increases, less added chloride is needed to depress the etch rate. In the low Baumé region (40° Bé) 0.46 M added chloride produces at most a slight depression, whereas in the high Baumé region (54° Bé) 0.11 M decreases the etch rate by about 10%, with further reductions at higher chloride concentrations [B].

Several other low-carbon steels were briefly investigated (Table 11). All etched at about the same rate as 1008 rimmed steel. Fig. 19 shows that 1005AK and 1008 rimmed steel have, within experimental accuracy, identical etch rates as a function of Baumé at 70.1 °C, and Fig. 20 shows that both show the sudden increase in surface roughness at about the same Baumé [B].

Table 11. Heterogeneous etch rates for various steels at 46.7° Bé and 70.1 °C, stirring speed 100 rpm [B]. (Printed as 10^{-8} cm s^{-1} in the original; see Editor's Note 2.)

Steel	Heterogeneous etch rate (10^{-6} cm s^{-1})
1008 rimmed	7.27 ± 0.25
1005AK	7.19 ± 0.10
1001AK	7.37 ± 0.17
FS (0.10 mm [4 mil] thick)	6.78 ± 0.17
ARMCO-IF	6.85 ± 0.21
AK-AOD	7.27 ± 0.22

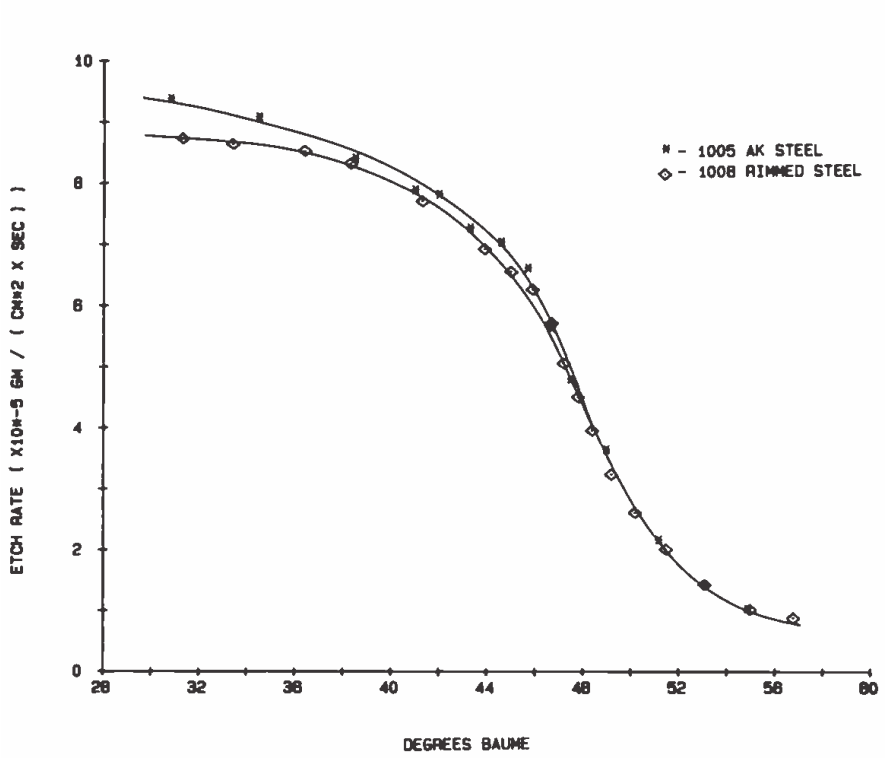


Fig. 19. Average etch rates (10^{-5} g cm^{-2} s^{-1}) for 1005AK and 1008 rimmed steel as a function of Baumé at 70.1 °C [B].

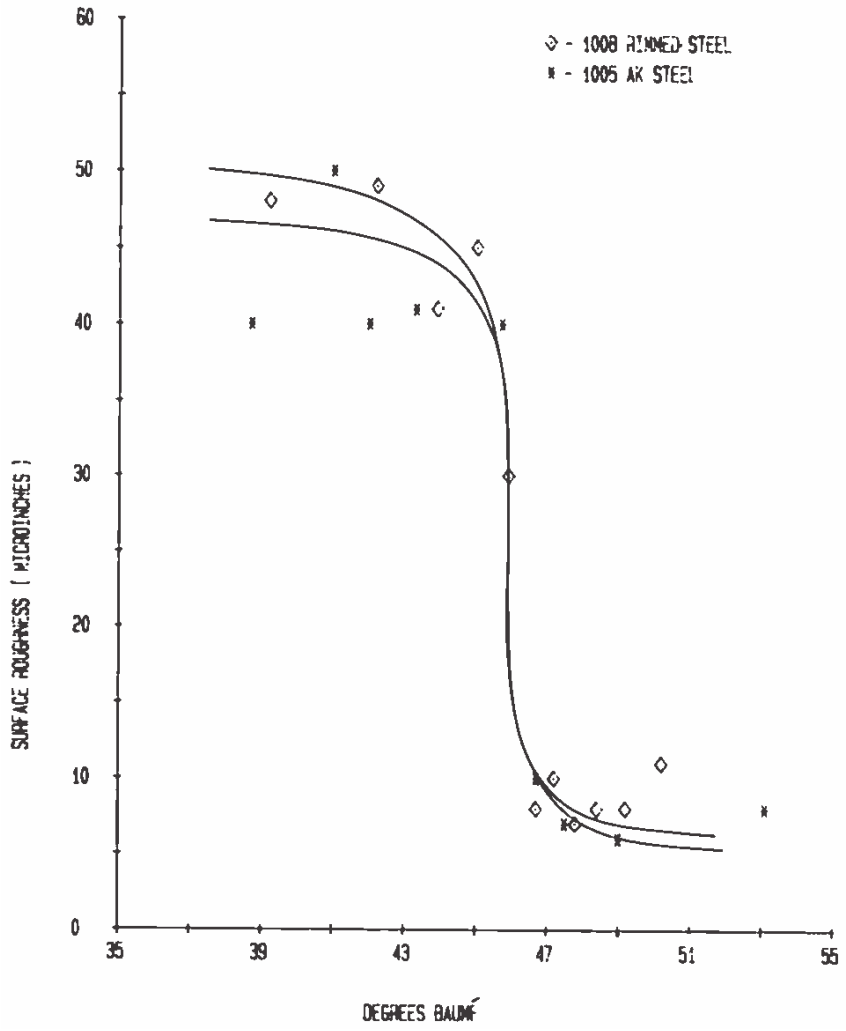


Fig. 20. Average surface roughness (microinches) for 1005AK and 1008 rimmed steel as a function of Baumé at 70.1 °C [B].

The viscosity of the etchant as a function of Baumé and temperature is summarized in Fig. 21. As expected, viscosity increases with Baumé, because more dissolved ferric chloride per unit volume requires more force per unit area to maintain the same velocity gradient [10]. Unexpectedly, a shoulder appears at high Baumé and high temperature; it grows into a peak and shifts to higher Baumé as the temperature decreases. Apparently the interactions between the ferric chloro species and the solvent reorganize over this Baumé range. When the Baumé was lowered from about 60° through this region, more water than usual was needed to lower the Baumé, suggesting a change in the partial molar volume of the solvent. This could come from changes in the hydration sphere of a ferric chloro species that alter its shape or size, requiring the bulk water to reorganize around the new species [B].

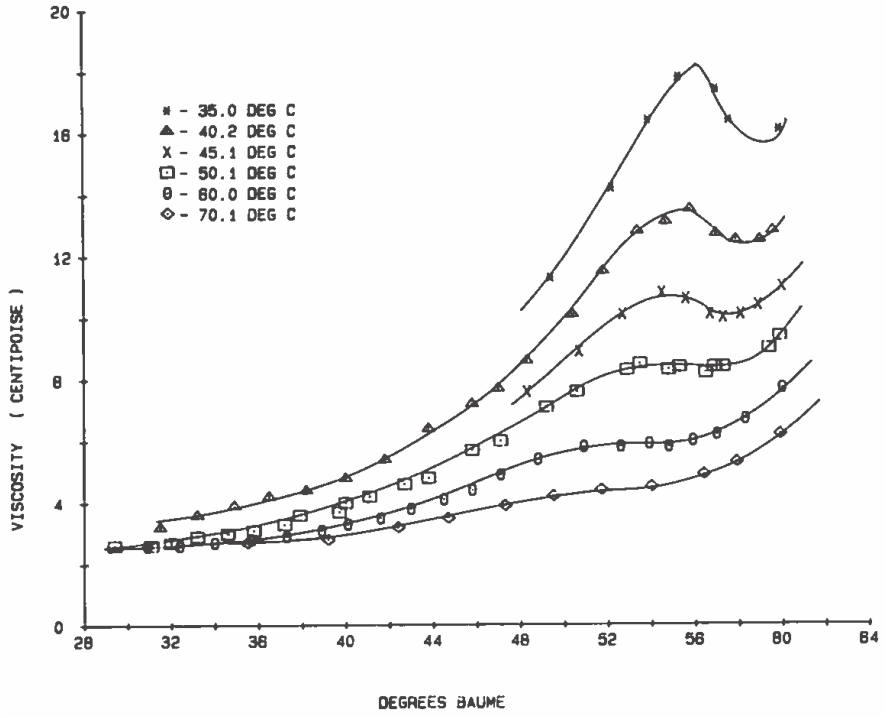


Fig. 21. Ferric chloride viscosity (centipoise; 1 cP = 1 mPas) as a function of Baumé and temperature (35.0–70.1 °C) [B].

4.5 Ferric chloride: mechanism

The shape of the curves in Fig. 15 suggests different mechanisms at low and high Baumé. In each of these regions the etch rate changes only gradually, indicating that one mechanism dominates; at intermediate Baumés the rate is a mixture of the two and changes rapidly with Baumé [B].

Low Baumé: transport-limited. At 32.0° Bé, $\Delta H^{\ddagger} = +3.07 \pm 0.13$ kcal/mol and $\Delta S^{\ddagger} = -25.3 \pm 0.3$ eu. Diffusion of small molecules in solvents of low viscosity typically shows enthalpies of activation of +1 to +4 kcal/mol [4–17 kJ/mol] [6]. The etch rate in this region also depends strongly on stirring (Fig. 22) and on the surface area of the sample (Table 12). These results suggest a rate limited by the encounter of ferric chloro species with the steel. Because the encounter rate contains contributions from both mass transport and diffusion, this process is termed “transport-limited” kinetics, following others [7]. The activation parameters are also very similar to those of the ferric perchlorate–perchloric acid system (Section 4.1, Table 7), in which transport of ferric ion from the bulk solution to the steel surface was proposed as the rate-determining step, so a similar step involving ferric chloro species is very plausible in the low Baumé region [B].

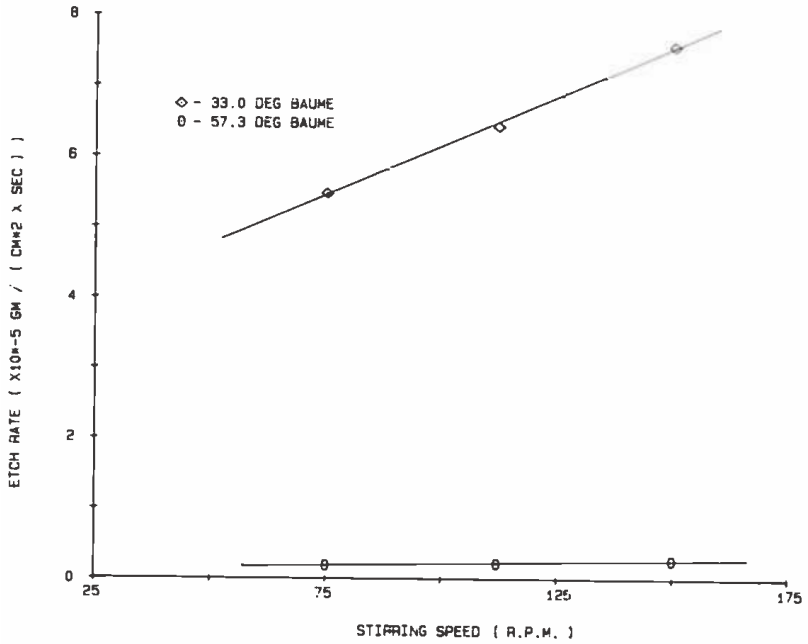


Fig. 22. Average etch rate (10^{-5} g cm^{-2} s^{-1}) as a function of stirring speed at 33.0° and 57.3° Baumé at 50.1 °C [B].

Table 12. Average etch rate as a function of steel surface area at 60.0 °C (stirring rate 100 rpm) [B].

Baumé	Surface area (cm^2)	Average etch rate (10^{-5} g cm^{-2} s^{-1})
34.3°	28.1	7.94 ± 0.34
34.3°	54.1	9.57 ± 0.10
55.9°	27.5	0.608 ± 0.009
55.9°	54.4	0.620 ± 0.012

High Baumé: surface-limited. The kinetic parameters could not be determined at a Baumé where the curves of Fig. 15 level out, because highly concentrated ferric chloride is difficult to keep in solution. The results at 57.0° Bé therefore include a slight contribution from transport-limited kinetics. Even so, $\Delta H^{\ddagger}$ = +10.9 ± 0.5 kcal/mol is too high for a diffusion-controlled reaction. If diffusion were important, the etchant viscosity would influence the etch rate [8]; but comparison of Fig. 15 with Fig. 21 shows viscosity has very little effect at high Baumé, particularly at higher temperatures, and the viscosity shoulder does not appear in the etch-rate curves. The enthalpy of activation instead falls in the range observed for processes dominated by adsorption; energies of adsorption generally range from about 9 to 100 kcal/mol [38–420 kJ/mol] [9]. The etch rate is also virtually independent of stirring rate (Fig. 22) and of sample area (Table 12). All these results are consistent with kinetics slower than transport-limited and point to a rate-limiting surface process: adsorption of reactant, reaction with surface iron atoms, desorption of products, or a combination. Since the present study cannot distinguish among these, the process is termed “surface-limited” kinetics [B].

Surface finish. An apparent physical manifestation of the change from surface-limited to transport-limited kinetics is the sudden appearance of a nonuniform coating of smut on the etched surface, which is believed to cause the increase in surface roughness seen in Fig. 16. Combining Figs. 15 and 16 gives Fig. 23, which shows the combinations of temperature and Baumé that give a smooth or a rough finish. Fig. 24 shows the difference pictorially: an approximately six-fold increase in roughness for a decrease of

only 1.5° Bé. Knowledge of the transition Baumé can be important in etching, for example, the apertures of a shadow mask [B], as Section 5 shows.

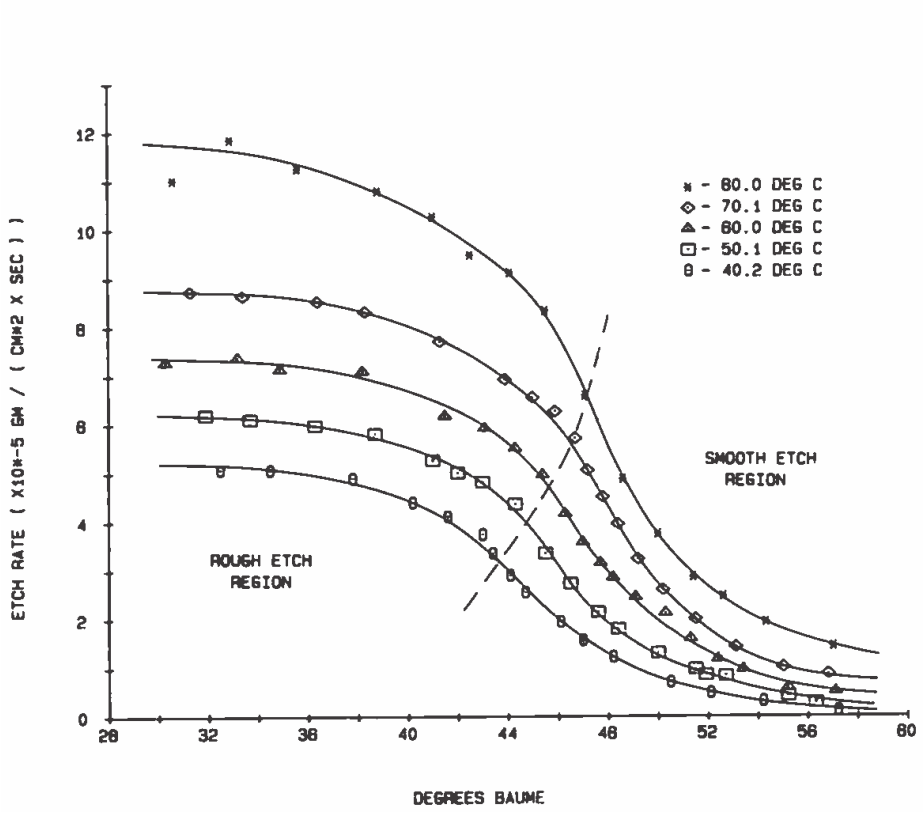


Fig. 23. Baumé and temperature combinations for smooth and rough etch. The parts of the curves to the right of the dotted line define the regions where smooth etch, and improved mask uniformity, are obtained [A, B].

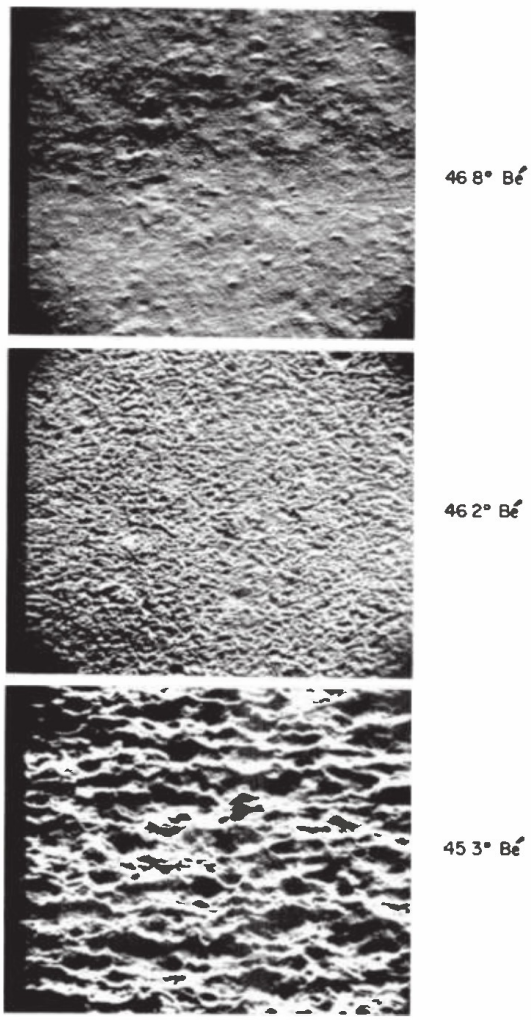


Fig. 24. SEM topography of 1008 rimmed steel etched at 80 °C at 46.8°, 46.2° and 45.3° Bé (top to bottom). Surface roughness 7 ± 1, 22 ± 2 and 45 ± 5 microinches [0.18, 0.56 and 1.14 µm]. Original photographs at 500× and 45° tilt [B].

Role of the ferric chloro species. One explanation for the change in mechanism with Baumé is a change in the identity of the reacting ferric chloro species. On raising the Baumé at 25 °C from 32° to 61°, the ferric concentration increases from 2.3 to 6.8 M. Raman, ESR and solution x-ray diffraction studies of concentrated ferric chloride [11–13] show that the principal species changes over this range, although the identities are interpreted somewhat differently by each group. From these studies and equilibrium data [14, 15], three species appear to be involved. At low concentration both $FeCl_2(H_2O)_4^+$ and $FeCl_3(H_2O)_3$ are present, the former probably in greater amount. As the Baumé increases, $FeCl_3(H_2O)_3$ becomes predominant and $FeCl_2(H_2O)_4^+$ declines, while $FeCl_4^-$ begins to appear and becomes predominant at high concentration; its formation is enhanced by added chloride [11]. Two of these species are ions of equal but opposite charge and the third is neutral, and each has a different relation to its counter-ion. Together the species present determine the adsorption behavior of the electrical double layer between the steel and the solution [16]. Changing or removing the charge on the reacting species would be expected to change the rate of adsorption profoundly; if $FeCl_4^-$ slows adsorption sufficiently, the mechanism changes from transport-limited to surface-limited. The effect of added chloride supports this: chloride inhibits the etch rate more strongly as the Baumé rises (Table 10), just where added chloride most enhances $FeCl_4^-$ formation [B].

Comparison with stainless steel. Allen and co-workers [17] spray-etched annealed AISI 304 stainless steel in ferric chloride (30–45° Bé at 30 and 50 °C). On lowering the Baumé they found the etch rate rose to about 38–42° Bé, leveled off, and rose again to a maximum at about 33–34° Bé, which they ascribed to a change of mechanism; the low-carbon steels show no such inflection. For stainless steel the roughness rose smoothly as the Baumé decreased, more so at lower temperature, whereas the low-carbon steel shows an abrupt rise, more marked at higher temperature. Both steels show a similar decrease in etch rate as free acid increases (at 40.2° Bé), but for stainless steel the roughness could be changed drastically by the free acid, whereas 1008 rimmed steel shows no dependence of roughness on free acid near its transition Baumé. Significant alloying elements (19% Cr, 10% Ni) can thus change drastically how a material etches in ferric chloride, so conclusions drawn for one material may not apply to another. (Allen et al. used spray etching; this is not believed to be a major cause of the differences.) [B]

5. Aperture Geometry and Etch-Process Design

Besides metallurgy, mask and aperture uniformity are determined during etching by equipment configuration, process conditions and artwork image-size design. For entertainment masks these parameters are well established for efficient high-yield production. Extensive tests on pilot and manufacturing equipment showed, however, that they must be modified for small-aperture, fine-pitch data-display masks [A].

5.1 Entertainment and data-display aperture geometry

Fig. 25a shows the typical finished aperture geometry of an entertainment mask, which gives good visual uniformity, process control and electron-beam clearance. Its critical features are a large screen-side opening, with 75 to 80% of the etching done from the screen side, and a swept-back surface where the gun- and screen-side openings meet. This geometry provides slowly changing surfaces for good process control during etching, and the smooth, swept-back opening that defines the beam gives good visual uniformity. The openings are large enough to prevent undesirable surface light reflections during mask inspection, and the finished dimensions keep the required artwork image sizes well within state-of-the-art limits [A].

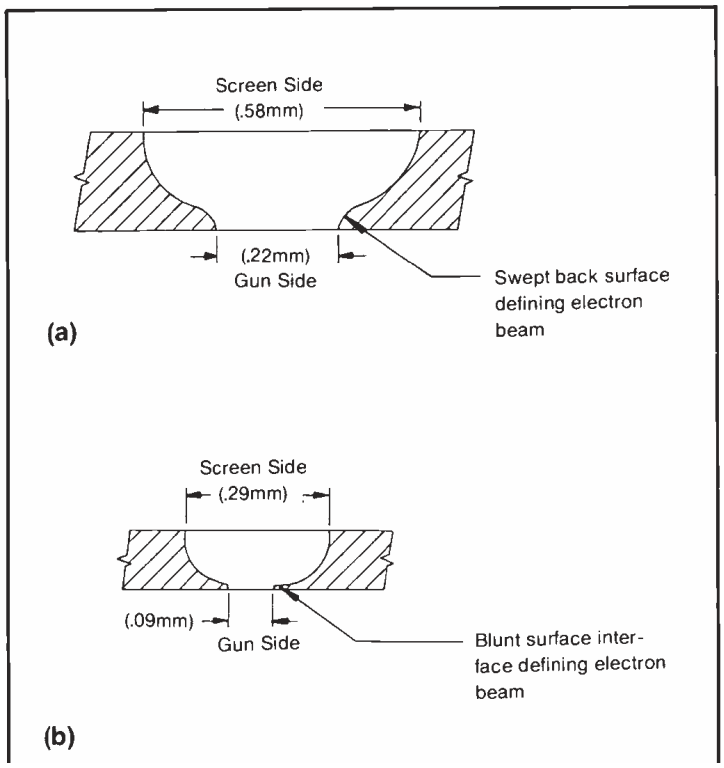


Fig. 25. Aperture geometry for (a) entertainment and (b) data-display masks. (a) Screen-side opening 0.58 mm, gun-side opening 0.22 mm, swept-back surface defining the electron beam. (b) Screen-side opening 0.29 mm, gun-side opening 0.09 mm, blunt surface interface defining the electron beam. The data-display geometry has smaller screen-side openings, deeper screen-side etching and a blunter surface where the openings meet [A].

Initial attempts to etch data-display masks with entertainment-mask parameters failed because of poor mask uniformity. Pilot tests showed that this was related to the data-display aperture geometry: the gun and screen openings, and the geometry of the surfaces where they meet during etching, caused a nonuniform appearance, aggravated by artwork image sizes outside entertainment-mask practice. Fig. 25b shows the empirically determined preferred geometry for data-display masks. Its distinguishing features are (1) small screen-side openings, because of the fine pitch; (2) 85 to 90% of the etching done from the larger screen-side opening; (3) a blunt surface, where the gun- and screen-side openings meet, that defines the electron beam; and (4) a screen-side opening "hollowed out" to minimize surface light reflections that could affect mask uniformity [A].

5.2 Single-step etch modifications

Two changes to the entertainment etching process were needed: more screen-side etching (to reduce surface reflections and give the desired beam clearance), and a different geometry of the gun- and screen-side surfaces where they intersect, since that intersection ultimately defines the beam [A].

Increased screen-side etching. Equipment modification was the most effective way to increase screen-side etching. The most critical part of the process takes place before the gun- and screen-side surfaces meet ("breakthrough"); after breakthrough the intersecting surfaces are cleaned out and no further penetration from the screen side alone is possible. The equipment was therefore modified to change the ratio of gun-side to screen-side etching *before* breakthrough. On the production line, the gun-side nozzles were changed to reduce the etchant flow rate, while extenders on the screen-side spray manifolds moved those nozzles closer to the strip. Pressures on both sides were adjusted for adequate,

uniform coverage; equipment and spray pressures after breakthrough were not changed. These modifications gave the desired increase in screen-side etching without unmanageable side effects [A].

Modified openings. Pilot etching tests on entertainment masks, run to find the effect of etchant temperature and concentration on aperture geometry, showed that at particular temperatures and concentrations the intersecting openings resembled the configuration desired for data-display masks. Those ranges were undesirable for entertainment-mask production because they would reduce production rates significantly, but they were acceptable for data-display masks. Laboratory tests on steel surface roughness (Section 4) showed that the improved-uniformity ranges coincided with the smooth-etch regions of Fig. 23. An optimum temperature–concentration combination was selected on this basis, and tests confirmed that it gave a more desirable data-display aperture geometry and improved mask uniformity. Work was continuing to improve the single-step process further, and two-step etching was being explored in parallel [A].

5.3 Two-step (precision) etching

Several factors set the minimum acceptable aperture that can be etched in a given thickness of material. There is a practical limit to the smallest clearly defined developed resist image, directly related to the artwork image size. Etching also proceeds laterally under the resist opening as the material is etched in depth; in practice the lateral rate is 60 to 80% of the depth rate. Even after the two sides meet, etching must continue to produce the desired opening, which further enlarges the minimum well-defined aperture (Fig. 26) [A].

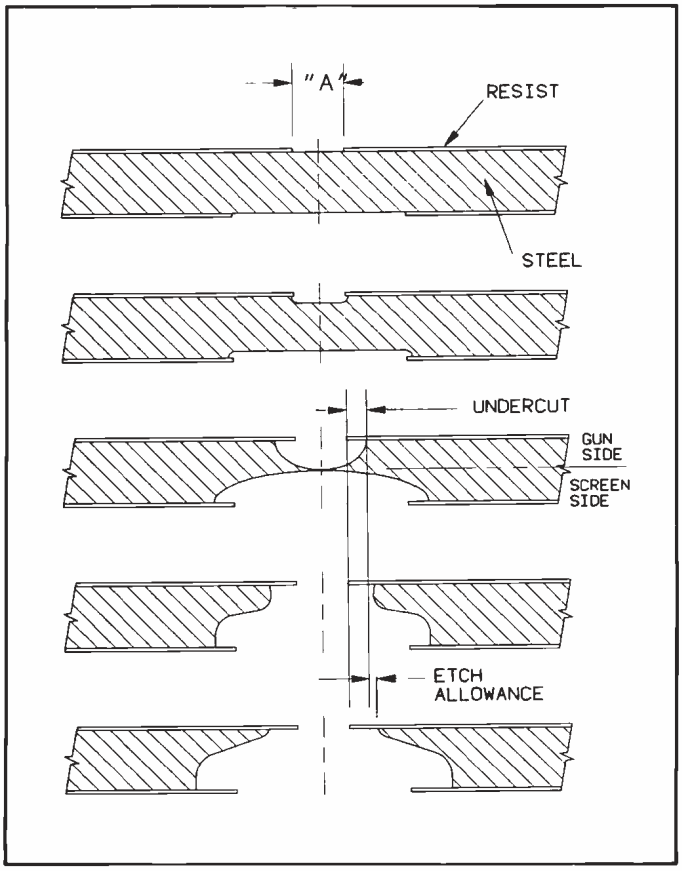


Fig. 26. Progression of etching. The sections show idealized steps in forming an etched aperture; the key features are undercut, etch depth and etch allowance [A].

Etching that extends beyond the stencil opening is called “undercut,” and it decreases as the etch depth decreases. A small minimum opening that closely matches the stencil can therefore be obtained by etching to a minimum depth from the small-opening side, which faces the electron gun and defines the opening through which the beam passes. In single-step etching this is done by retarding the etching from the small side while increasing it from the large side. The smallest clearly defined opening obtainable by single-step etching is about 70% of the material thickness. Smaller apertures need more elaborate procedures [A].

To meet this need, a shield-like chamber was designed and built within the etch chamber [3] (Fig. 27). The enclosure keeps etchant from the small-opening side until the large-opening side has been etched to a predetermined depth. The strip then moves out of the enclosure and is etched from both sides simultaneously, with the large-opening side given a “head start.” The prolonged etching of the large side effectively reduces the material thickness, so that only minimal etching of the small side is needed before the two sides meet, which significantly reduces the undercut of the small-side images [A].

The patent [3] gives the design. The strip, low-carbon cold-rolled steel about 21.4 in [543 mm] wide and 0.15 mm thick, moves through a closed etching chamber about 90 in [2.3 m] long, with five oscillating spray tubes above and five below that sweep etchant across both faces at 10–40 psi [69–276 kPa]. A solid wall of clear acrylic about ¼ in [6 mm] thick (or opaque fiberglass-reinforced vinyl ester) lies above the strip over the first 60 in [1.5 m] of the chamber, more than half its length, and intercepts the top sprays. With the strip it forms a stationary shielding chamber over the O-side (gun side), while the R-side (screen side) is sprayed from below throughout. The strip edges run in U-shaped side seals, a box-shaped upper member and an angle-shaped lower member, whose narrow, winding path keeps the bottom spray out of the shielding chamber; rollers within the seals stop the strip from sagging. A flexible baffle riding on the strip can close the exit end, the shielding chamber can be held at a slightly higher gas pressure than the etching chamber, and the shield can be moved along the strip to adjust the ratio of shielded to unshielded time. A tighter seal of stacked flexible sheets pressing the strip edge, and a version for vertical strip with drained lower seals, are also described. Line speeds of 12–18 in/min [0.30–0.46 m/min] were used in the tests, and 12–85 in/min [0.30–2.2 m/min] is practical, with mass production at the upper end. Because the shield is stationary, no etch-resistant coating or plastic sheet has to be applied to and removed from the moving strip, as in earlier forms of the same principle [24].

Table 13 gives the patent’s test results. “Delta” is the lateral etching: the difference between the minimum etched opening and the O-side stencil opening. With the shield, delta fell from 51–64 µm to 18–23 µm for round apertures and from 71–76 µm to 38–43 µm for slits, even though the shielded runs used the same or thicker strip.

Table 13. Lateral etching (“delta”) without (prior) and with (shielded) the O-side shielding chamber, cold-rolled steel strip. From US 4,389,279 [3]; 1 mil = 25.4 µm.

Run	Process	Strip thickness (mil) [µm]	Aperture	Minimum etched opening (mil) [µm]	O-side stencil opening (mil) [µm]	Delta (mil) [µm]
1	Prior	5.0 [127]	Round	5.4 [137]	2.9 [74]	2.5 [64]
2	Prior	4.0 [102]	Round	5.4 [137]	3.4 [86]	2.0 [51]
3	Shielded	6.0 [152]	Round	4.1 [104]	3.4 [86]	0.7 [18]
4	Shielded	5.0 [127]	Round	4.3 [109]	3.4 [86]	0.9 [23]
5	Prior	6.0 [152]	Slit	6.6 [168]	3.6 [91]	3.0 [76]

Run	Process	Strip thickness (mil) [µm]	Aperture	Minimum etched opening (mil) [µm]	O-side stencil opening (mil) [µm]	Delta (mil) [µm]
6	Prior	4.0 [102]	Slit	4.7 [119]	1.9 [48]	2.8 [71]
7	Shielded	6.0 [152]	Slit	5.1 [130]	3.6 [91]	1.5 [38]
8	Shielded	6.0 [152]	Slit	5.1 [130]	3.4 [86]	1.7 [43]

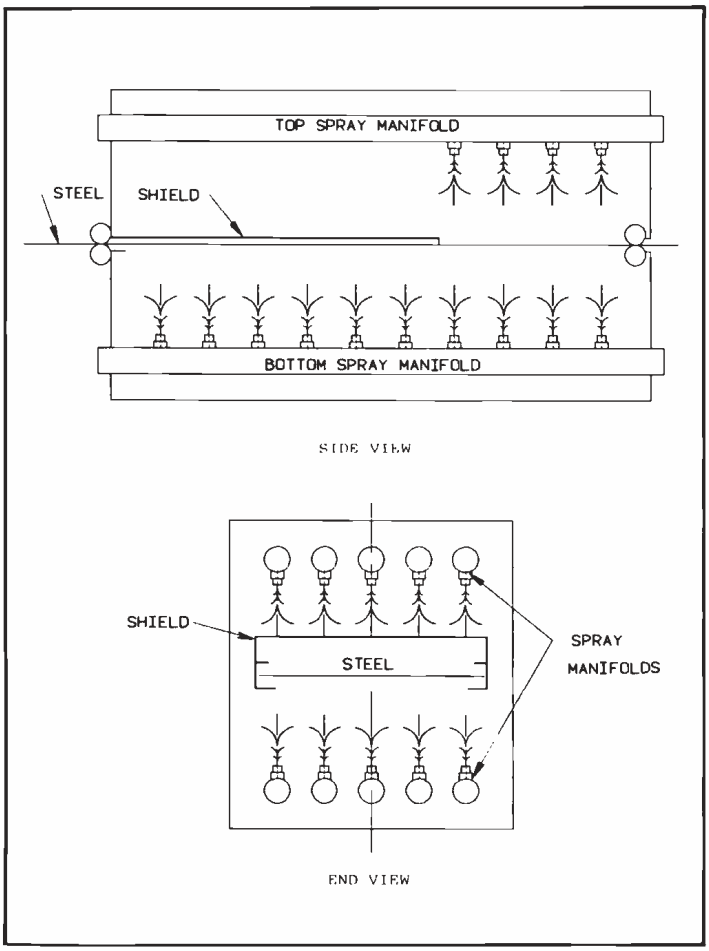


Fig. 27. Precision etch equipment and process (side and end views). A shield-type chamber over the small-opening side of the steel achieves very small apertures for ultra-high-resolution masks. This relatively simple modification has been effective in producing good-quality data-display masks [A].

Advantages of the two-step process that cannot be achieved with one-step etching [A]:

1. Minimum undercut occurs on the small-image side of the strip.
2. A smaller etch allowance (Fig. 26) is needed.
3. The etched aperture more closely approximates the artwork image.
4. The continuous process does not need an etch-resistant coating or other chemicals that retard etching.

5. Missing-stencil defects on the small-image side are less critical, because their enlargement during etching is much smaller than in one-step etching.
6. Existing production equipment can be converted to two-step etching quickly and at minimum expense.

Disadvantages [A]:

1. Productivity for a given etch-chamber length is significantly lower.
2. The large-side images undergo much greater undercut, which sometimes makes it difficult to keep adjacent apertures separate.
3. Production flexibility is lost, because two-step etching of entertainment masks is not economically practical.

Two-step etching will therefore be used in production only when demand justifies the higher cost of such a sophisticated mask [A].

6. Etching Invar Shadow Masks

This section was added in 2026. It draws on two later RCA/Thomson patents by the same Lancaster group [26, 27] and a 2017 conference paper [32]; it is not part of the 1984 papers.

6.1 Why Invar

Invar is an iron–nickel alloy containing about 36 weight percent nickel. Its coefficient of thermal expansion near room temperature is only about one-tenth that of low-carbon steel, and it is stronger. An Invar mask therefore changes dimension much less when the electron beams heat it during tube operation ("doming"), which would otherwise move the apertures out of register with the phosphor screen. It can also be made from thinner strip [26, 27]. With the growth of high-performance color picture tubes and color display tubes, the use of Invar in shadow masks increased significantly [27].

Invar masks are made by the same photofabrication sequence as steel masks (Section 2.1): registered resist stencils on both faces of the strip, spray etching in ferric chloride, then separation, annealing and forming. The RCA patent for Invar uses the shielded etching chamber of Section 5.3 (Fig. 28) [26]. The new element is the nickel in the alloy. Ferric ion oxidizes both metals,

$$Fe + 2\ FeCl_3 \rightarrow 3\ FeCl_2$$

$$Ni + 2\ FeCl_3 \rightarrow NiCl_2 + 2\ FeCl_2$$

and ferrous chloride is normally reoxidized to ferric chloride (for example by chlorine) and reused. Nickelous ion, in contrast, cannot oxidize iron or nickel and is not raised to a higher oxidation state by chlorine, so it simply accumulates. Left alone, the nickel content of a recirculating etchant would rise toward the composition of the alloy itself, about 35 mol% of the dissolved metal. Nickel chloride is inactive as an etchant: it dilutes the etchant, slows the etch and roughens the etched surface [26].

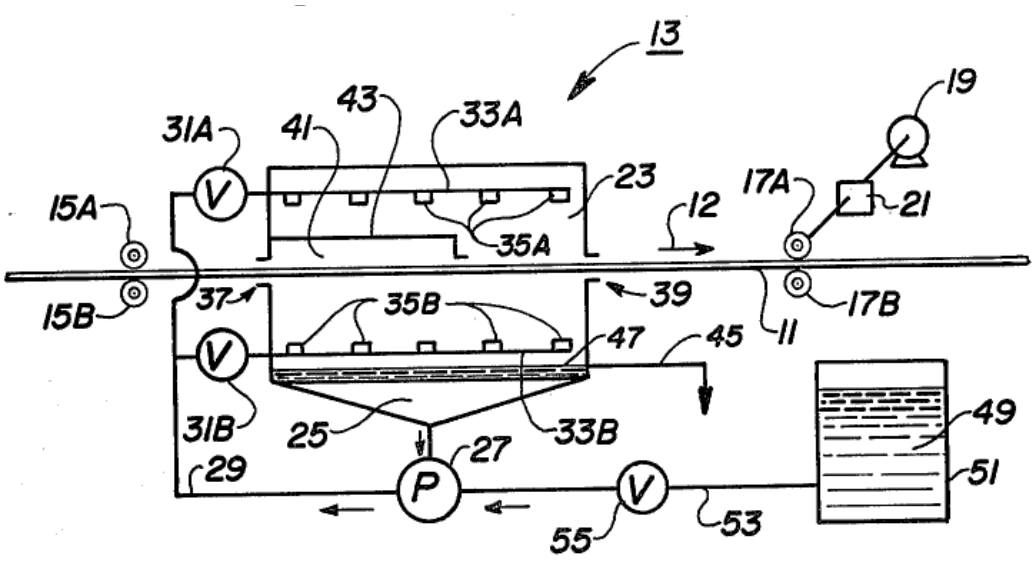


Fig. 28. Spray etching line for Invar strip, with the shielding chamber of Section 5.3 and a fresh-etchant feed and overflow for nickel control: 11 strip; 23 etching chamber; 25 sump; 27 pump; 33A, 33B upper and lower spray tubes; 41, 43 shielding chamber and wall; 45 overflow; 49, 51 fresh nickel-free etchant and reservoir. From US 4,482,426 [26].

6.2 Effect of nickel ion on smooth etching

Maynard, Moscony and Saunders, the authors of [B] and [C], extended their study of surface finish to Invar [26]. With nickel-free ferric chloride, Invar shows the same sharp transition from smooth to rough etch as the Baumé is lowered (Fig. 29). At 80 °C, the finish is about 5 microinches [0.13 µm] at 53° Bé and changes abruptly between 48.6° and 47.6° Bé to more than 10 microinches [0.25 µm]; at 40° Bé it exceeds 60 microinches [1.5 µm]. Unlike low-carbon steel, however, the Invar transition is essentially independent of temperature from 40 to 85 °C. For 1008 rimmed steel it moves from about 43° Bé at 40 °C to about 48° Bé at 80 °C, as in Fig. 23 [26].

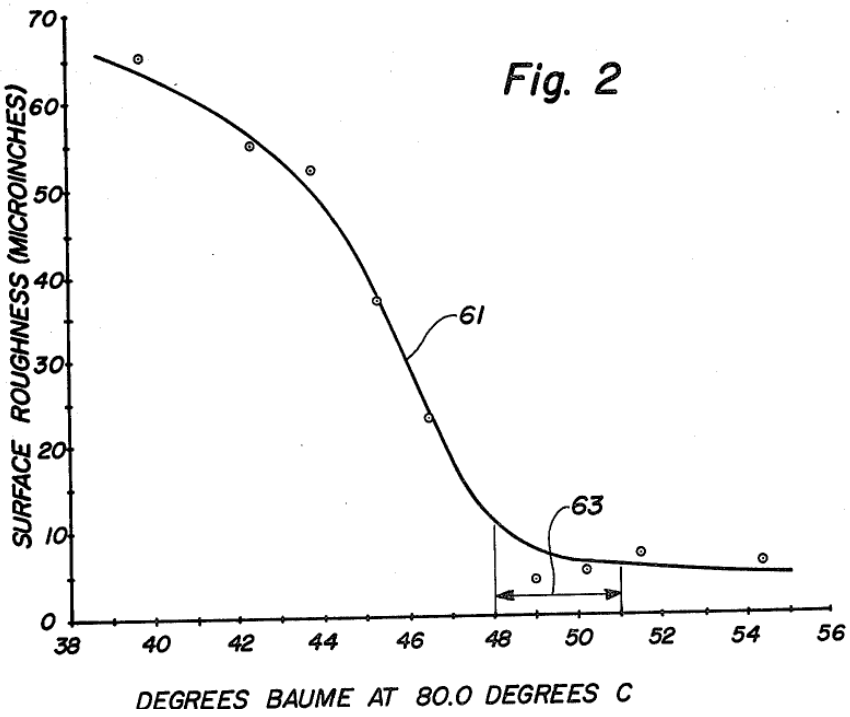


Fig. 29. Surface roughness (microinches; 1 µin = 0.0254 µm) of Invar etched in nickel-free ferric chloride as a function of Baumé at 80.0 °C. Arrow 63 marks the practical range of the method, 48.0–51.0° Bé. From US 4,482,426 [26].

Nickel ion in the etchant raises the Baumé needed for a smooth etch (Fig. 30). The minimum Baumé y for smooth etch, as a function of x, the nickel content in mol% of the total nickel plus iron in the etchant, is given empirically by

$$y = 47.824 + 0.337x - 0.0131x^2 + 0.00017x^3$$

which is also essentially independent of temperature in the usual etching range [26]. The required Baumé rises steeply at first, from 47.8° Bé with no nickel to 49.2° Bé at 5 mol% and 50.1° Bé at 10 mol%, then levels off near 51° Bé (Fig. E2, left). Since both nickel ion and higher Baumé reduce the etch rate, the most productive combination is the highest practical temperature, the lowest Baumé that still gives a smooth etch, and as little nickel as possible. In practice this means 70–85 °C, 48.0–51.0° Bé (SG 1.495–1.540), and 0–5 mol% nickel; about 85 °C is the upper practical temperature for production [26].

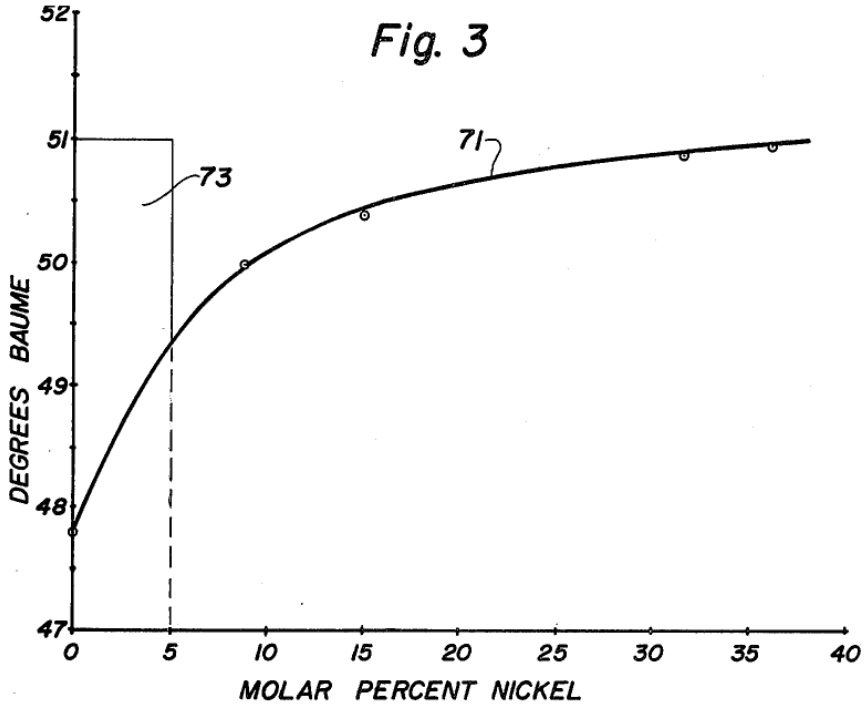


Fig. 30. Minimum Baumé required for a smooth etch (< 10 microinches [0.25 µm]) of Invar as a function of the nickel content of the etchant, in mol% of nickel plus iron. Area 73 is the practical operating range. From US 4,482,426 [26].

Fig. 31 compares this window with that of an earlier Japanese patent for etching nickel–iron masks (Oka et al. [25]), which required free hydrochloric acid, 40–70 °C, no more than 15 weight percent total nickel and ferrous iron, and 43–51° Bé depending on temperature. The two regions abut but do not overlap. Etchants within the RCA region gave a smooth etch, well-formed apertures and good visual uniformity, whereas two etchants inside the earlier region gave rough etch and poor visual uniformity on similar Invar strip. The earlier patent did not recognize the effect of nickel ion on etch rate or roughness [26].

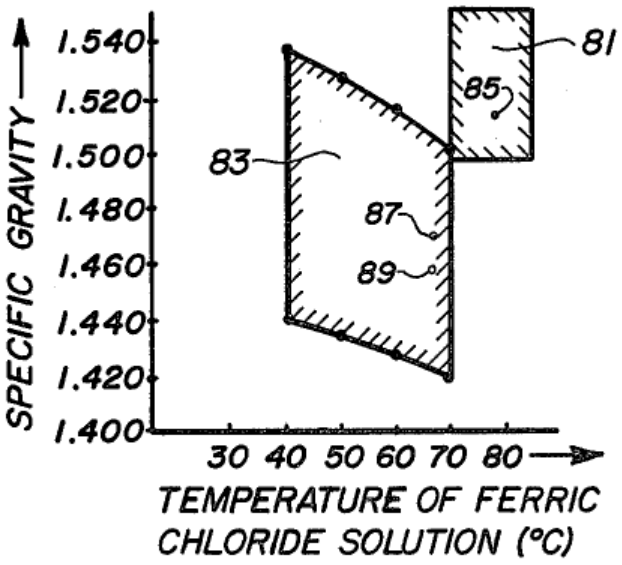


Fig. 31. Etchant temperature and specific gravity for Invar: area 81, the RCA method (70–85 °C, SG 1.495–1.540); area 83, the method of Oka et al. [25]. Point 85 gave smooth etch; points 87 and 89 gave rough etch. From US 4,482,426 [26].

Table 14. Ferric chloride etching conditions for Invar shadow masks.

	Oka et al. [25]	Maynard, Moscony and Saunders [26]
Temperature	40–70 °C	70–85 °C (about 80 °C typical)
Baumé (SG)	43–51° Bé (1.420–1.540), depending on temperature	48.0–51.0° Bé (1.495–1.540); 49° Bé preferred
Nickel limit	≤ 15 wt% total Ni + Fe^{2+}	0–5 mol% Ni of Ni + Fe
Free HCl	Required, controlled	Not specified
Result on Invar	Rough etch, poor uniformity	Smooth etch, good uniformity

The patent gives one production figure: on a particular etch line at 80 °C and 49° Bé, Invar etched at about 2.0×10^{-4} g cm^{-2} s^{-1} for a 25-inch mask pattern [26]. That is about 15 µm per minute from each face, about twice the fastest beaker rates of Section 4.3 (Fig. 15), as expected under vigorous spray. The strip, 0.15 mm thick and about 21.4 in [543 mm] wide, ran at about 0.3–1.5 m/min [26].

6.3 Controlling and recovering the nickel

Feed and bleed. The simplest way to hold the nickel down is to bleed part of the etchant continuously from the sump through an overflow and replace it with nickel-free ferric chloride (Fig. 28). The etch rate then stays essentially that of pure ferric chloride [26]. The patent gives an overflow rate for its example line (see Editor's Note 8 on its magnitude). Further economy comes from regenerating the overflow, removing the nickel and returning low-nickel ferric chloride to the fresh-etchant reservoir. Electrolytic cells divided by an ion-exchange membrane, which plate the nickel out as metal for salvage, are suggested for this [28, 29].

Solvent extraction. By the 1990s, Invar masks were in wide use, and spent Invar etchant, replaced when it reached about 5% nickel, was costly both in line downtime and in disposal of the mixed iron–nickel waste. Moscony and Cushman, at Thomson Consumer Electronics in Lancaster, patented a liquid–liquid extraction that separates ferric chloride from nickel chloride so that the ferric chloride can be reused [27]. It relies on the chloro-complex chemistry of Section 4.5. In concentrated hydrochloric acid, iron(III) is present mainly as $FeCl_4^-$, which a long-chain secondary amine in its hydrochloride form extracts into an organic phase as an ion pair. Nickel(II) forms no such anionic complex and stays in the water. Earlier extractants were less suitable. Tributyl phosphate extracted only about 63% of the iron in a laboratory comparison, and 4-methyl-2-pentanone (98%) has a flash point of 13 °C, carries over into the recovered ferric chloride and needs very concentrated acid [27, 30].

The extractant is Amberlite LA-2 amine (187 g/L) with isodecanol (Exxal 10, 187 g/L), which prevents a third phase from forming, in aromatic kerosene (Exxon Aromatic 150). It is first converted to the amine hydrochloride with HCl. The circuit has two countercurrent extraction stages and two stripping stages of mixer–settlers (Fig. 32). In the example, 100 mL of spent etchant (270.2 mg/mL Fe and 15.5 mg/mL Ni, about 5.2 mol% Ni) is mixed with 35 mL of 12 M HCl to make the feed (200.1 mg/mL Fe, 11.4 mg/mL Ni). The extraction isotherm (Table 15, Fig. 33) with an organic-to-aqueous ratio of 10/1 predicts that two stages load the organic phase to 20.9 mg/mL Fe (20.7 measured) and leave a raffinate of only 1.7 mg/mL Fe, removing about 99% of the iron. The nickel stays in the raffinate, from which it can be recovered as a salable product: the organic phase picks up only 0.0014–0.0025 mg/mL Ni. The iron is stripped from the organic phase with 1 N HCl. At O/A = 1/1, two stages give an aqueous ferric chloride of about 20.7 mg/mL Fe and remove 95.9% of the iron; at O/A = 2/1, four stages give about 42 mg/mL Fe

and remove 96.6%. The stripped organic phase is recycled, and the aqueous ferric chloride is evaporated back to etchant strength, or to dry salt [27].

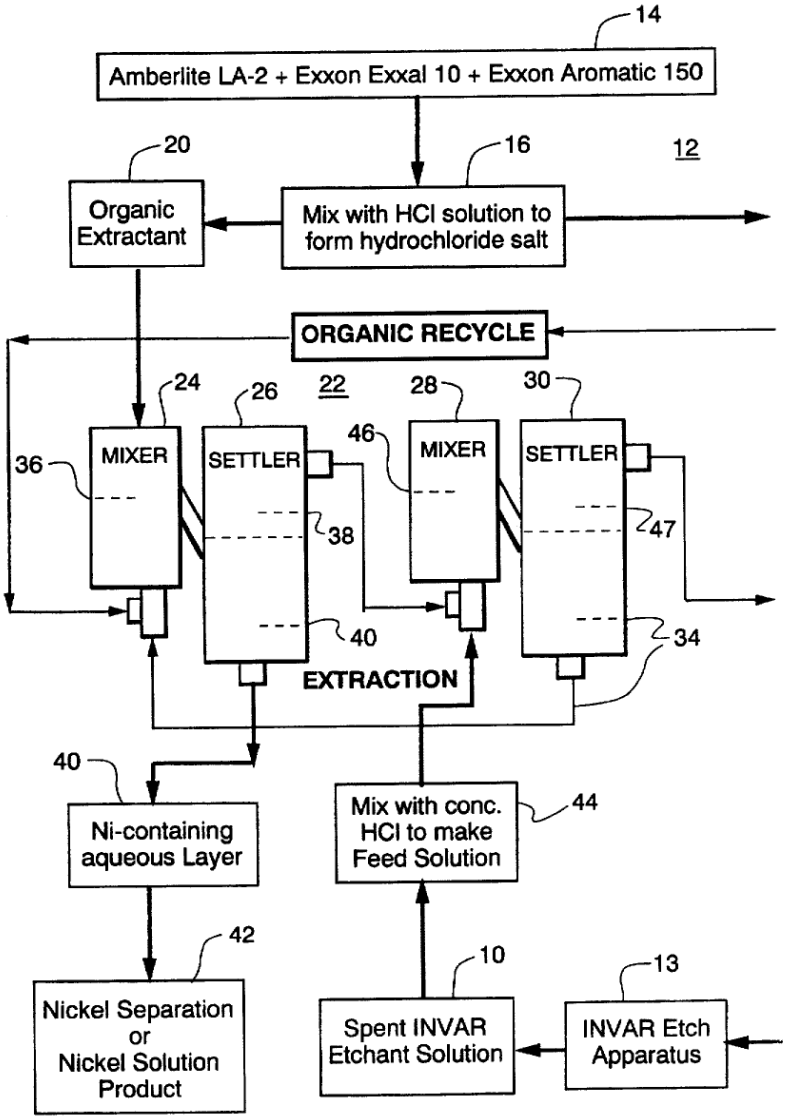


Fig. 32. Extraction section of the solvent-extraction process for spent Invar etchant: amine extractant 14 converted to hydrochloride 20; two mixer–settler stages 24–30; feed 44 (spent etchant 10 plus concentrated HCl); nickel-containing raffinate 40 to nickel recovery 42. From US 5,718,874 [27].

Table 15. Extraction isotherm for spent Invar etchant with Amberlite LA-2 hydrochloride in aromatic kerosene. From US 5,718,874 [27].

O/A	Fe, aqueous (mg/mL)	Fe, organic (mg/mL)	Ni, aqueous (mg/mL)	Ni, organic (mg/mL)
11.1/1	15.5	13.8	15.7	0.0016
7.4/1	34.2	18.4	15.8	0.0014
3.7/1	91.5	27.1	14.8	0.0017
1.5/1	153.2	33.8	14.0	0.0021

O/A	Fe, aqueous (mg/mL)	Fe, organic (mg/mL)	Ni, aqueous (mg/mL)	Ni, organic (mg/mL)
1/1	165.7	36.4	13.8	0.0025
Stripped organic	—	0.93	—	0.0007
Feed solution	200.1	—	11.4	—
Spent etchant	270.2	—	15.4	—

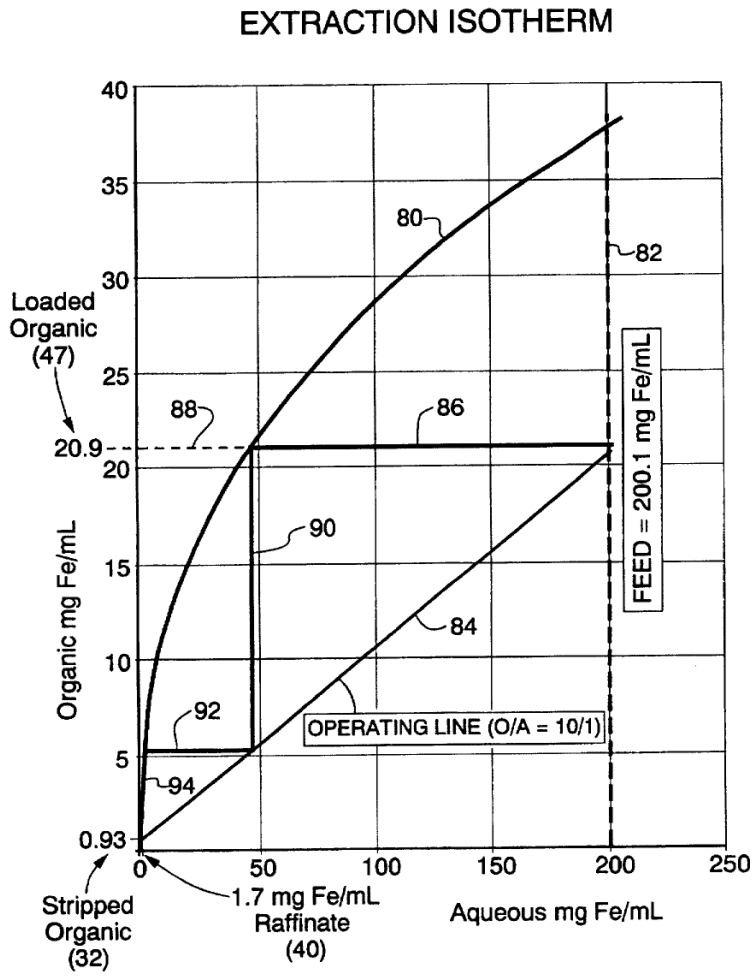


Fig. 33. Extraction isotherm (curve 80) with an operating line for O/A = 10/1. Two steps reduce the iron in the feed from 200.1 to 1.7 mg/mL and load the organic phase to 20.9 mg/mL. From US 5,718,874 [27].

6.4 Thin Invar masks today

Invar shadow masks outlived the color picture tube. Fine-metal masks for evaporating the colored layers of OLED displays are made of thin Invar, again because of its low expansion, and spray etching in ferric chloride remains the usual way to make them, alongside electroforming and laser machining [32]. Moon et al. [32] spray-etched 30 µm Invar foil through a 120 × 80 µm opening in a laminated dry-film resist (Hitachi, laminated at 110 °C and 1 m/min, exposed for 90 s and developed in 4 wt% developer). They used 30 wt% $FeCl_3$ at 35 °C and 0.08 MPa from one nozzle below a reciprocating sample (Table 16); the effect of spray characteristics on etching Invar in $FeCl_3$ has been studied separately [31].

Table 16. Spray-etching conditions of Moon et al. [32].

Condition	Value
Foil	Invar (64 Fe–36 Ni), 30 µm thick
Resist opening	120 × 80 µm (dry film)
Etchant	30 wt% $FeCl_3$ (about 33° Bé)
Temperature	35 °C
Spray pressure	0.08 MPa
Etch time	1–5 min, one side

The depth was 15.9 µm after 1 minute, then 18.7, 20.5 and 23.6 µm after 2, 3 and 4 minutes, and the foil was etched through at 5 minutes (Fig. 34; Fig. E2, right). The hole entrance grew steadily by lateral etching, to 119 × 91.6 µm at breakthrough. Longer etching would have merged neighboring holes and lifted the dry film. With the same 5-minute etch, they made a uniform 5.5-inch mask (Fig. 35) [32].

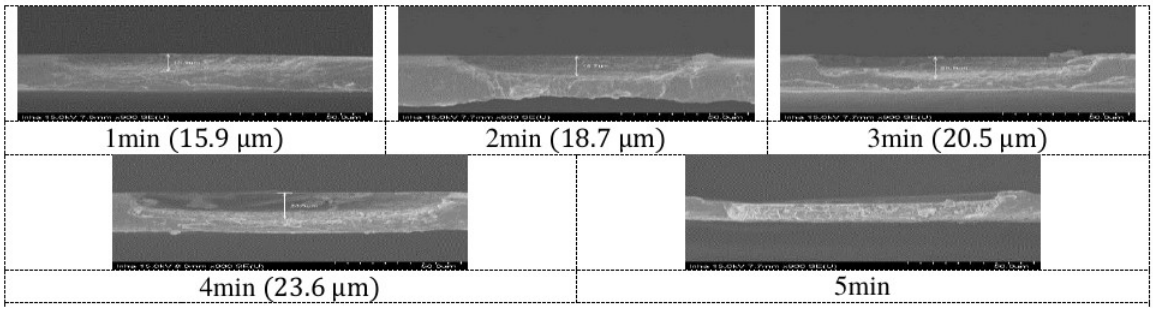


Fig. 34. SEM cross sections of the etch depth in 30 µm Invar after 1 min (15.9 µm), 2 min (18.7 µm), 3 min (20.5 µm), 4 min (23.6 µm) and 5 min (through). From Moon et al. [32], CC BY 3.0.

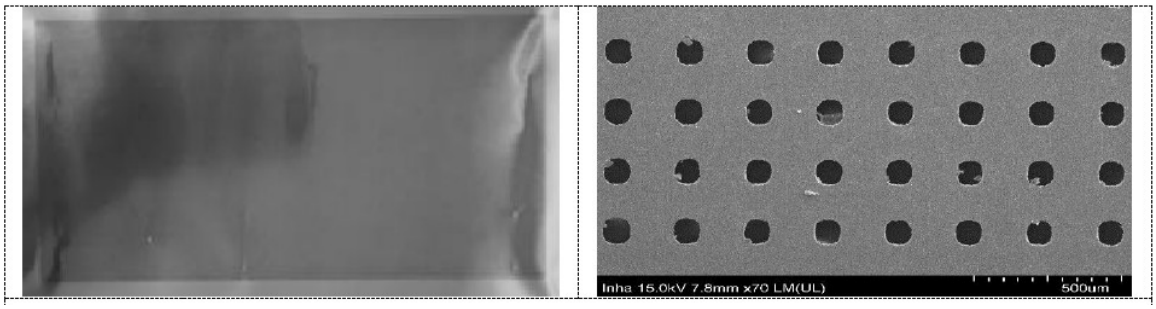


Fig. 35. 5.5-inch Invar shadow mask (left) and its hole array (right; scale bar 500 µm). From Moon et al. [32], CC BY 3.0.

These conditions lie far from the RCA window: a dilute etchant (about 33° Bé against 48–51° Bé) at low temperature. On the RCA results, both put the etch in the rough, transport-limited region (Figs. 23, 29 and 30); see Editor's Note 9.

7. Summary and Conclusions

1. **Steel.** Aluminum-killed steel, with lower and uniformly distributed impurities, gives cleaner aperture edges than rimmed steel and can be annealed free of yield-point elongation, giving

more uniform formed masks. Low-carbon steels, rimmed or killed, etch at essentially the same rate in ferric chloride.

2. **Model-system kinetics.** In ferric perchlorate–perchloric acid, loss of Fe^{3+} is first order in ferric ion, proportional to steel area, increased by stirring, roughly inversely proportional to viscosity, independent of ferrous ion and of acid above 0.05 N, and has a low enthalpy of activation (about 2.8 kcal/mol [12 kJ/mol]). The rate is limited by the encounter of the ferric hexaaquo ion with the steel, followed by fast electron transfer through an adsorbed Fe(I) intermediate.
3. **Ferric chloride kinetics.** Etching of 1008 rimmed steel in ferric chloride involves two competing mechanisms: transport-limited kinetics at low Baumé (below about 40° Bé) and surface-limited kinetics at high Baumé (above about 54° Bé), with mixtures in between. High chloride concentrations inhibit etching, particularly at high Baumé, consistent with the growing role of $FeCl_4^-$, and have no noticeable effect on roughness.
4. **Surface finish.** Roughness depends on Baumé and, to a lesser extent, temperature. It rises abruptly below a transition Baumé that increases with temperature, coinciding with the appearance of smut, and rough etching contributes to nonuniformity in the etched part.
5. **Process design for data-display masks.** Operating in the smooth-etch region, shifting the gun-side/screen-side etch ratio before breakthrough toward the screen side, and—for the finest masks—a two-step precision etch with a shielded first stage which in patent tests cut lateral etching of the gun-side openings by roughly a factor of two to three, allowed RCA VCDD to produce high-resolution data-display masks with good uniformity using relatively minor changes to existing equipment.
6. **Invar.** For Fe–36Ni Invar masks, nickelous ion accumulates in the etchant, slowing the etch and raising the Baumé needed for a smooth finish (47.8° Bé with no nickel, 49.2° Bé at 5 mol%). Unlike that of low-carbon steel, the smooth/rough transition for Invar does not depend on temperature. Production conditions are therefore 70–85 °C, 48–51° Bé and no more than 5 mol% nickel. The nickel is held down by bleeding and replacing etchant, and the spent etchant can be regenerated electrolytically or by amine solvent extraction of $FeCl_4^-$, which removes about 99% of the iron from the nickel in two stages.

Further challenges were expected with the introduction of high-definition television, and color data-display tubes were seen as a promising and growing business [A].

Acknowledgments

The authors of [B] thank Dale Goodman for measuring surface roughness and JoAnn Wolfe for the SEM topography photographs.

References

1. J. J. Moscony, “Process Requirements for a New Generation of Precision In-line Shadow Masks,” *RCA Engineer* **25**, No. 2 (1979).
2. R. B. Maynard, J. J. Moscony and M. H. Saunders, “A Study of the Etching Kinetics of Low Carbon Steel Using the Ferric Perchlorate–Perchloric Acid System as a Model,” *RCA Review* **45**, p. 58 (March 1984). (Source [C]; Section 4.1.)

3. D. M. Weber and R. A. Alleman, “Method of Etching Apertures into a Continuous Moving Metallic Strip,” U.S. Patent 4,389,279 (June 21, 1983). (Printed as 4,309,279 in [A]; see Editor’s Note 5.)

4. R. G. Wilkins, *The Study of Kinetics and Mechanism of Reactions of Transition Metal Complexes*, pp. 79–81, Allyn and Bacon, Boston (1974).

5. V. Fried, H. F. Hameka and U. Blukis, *Physical Chemistry*, p. 64, Macmillan, New York (1977).

6. S. W. Benson, *The Foundations of Chemical Kinetics*, p. 499, McGraw-Hill, New York (1960); D. Shooter, in *Comprehensive Chemical Kinetics*, Vol. 1, p. 253, C. H. Bamford and C. F. H. Tipper, eds., Elsevier, Amsterdam (1969).

7. H. R. Rogers, C. L. Hill, Y. Fujiwara, R. J. Rogers, H. L. Mitchell and G. M. Whitesides, “Mechanism of Formation of Grignard Reagents. Kinetics of Reaction of Alkyl Halides in Diethyl Ether with Magnesium,” *J. Am. Chem. Soc.* **102**, p. 217 (1980).

8. W. Jost, *Diffusion in Solids, Liquids and Gases*, p. 2, Academic Press, New York (1952).

9. W. J. Moore, *Physical Chemistry*, 4th ed., p. 496, Prentice-Hall, Englewood Cliffs, NJ (1972).

10. V. Fried, H. F. Hameka and U. Blukis, *Physical Chemistry*, p. 710, Macmillan, New York (1977).

11. W. L. Marston and S. F. Bush, “Raman Spectral Investigation of the Complex Species of Ferric Chloride in Concentrated Aqueous Solution,” *Appl. Spectrosc.* **26**, p. 579 (1972).

12. M. Magini and T. Radnai, “X-Ray Diffraction Study of Ferric Chloride Solutions and Hydrated Melt. Analysis of the Iron(III)–Chloride Complexes Formation,” *J. Chem. Phys.* **71**, p. 4255 (1979); G. Giubileo, M. Magini, G. Licheri, G. Paschina, G. Piccaluga and G. Pinna, “On the Structure of Iron(III) Chloride Solutions,” *Inorg. Chem.* **22**, p. 1001 (1983).

13. D. L. Wertz and M. L. Steele, “Coordination of Fe^{3+} in Concentrated Aqueous Solutions with Chloride Ligands,” *Inorg. Chem.* **19**, p. 1652 (1980); D. L. Wertz and M. D. Luter, “Evolving Cation Coordination in Aqueous Solutions Prepared from Iron(III) Chloride Hexahydrate,” *Inorg. Chem.* **20**, p. 3118 (1981).

14. G. A. Gamlen and D. O. Jordan, “A Spectroscopic Study of the Iron(III) Chloro-Complexes,” *J. Chem. Soc.*, p. 1453 (1953).

15. Y. Strahm, R. C. Patel and E. Matijević, “Thermodynamics and Kinetics of Aqueous Iron(III) Chloride Complex Formation,” *J. Phys. Chem.* **83**, p. 1689 (1979).

16. A. W. Adamson, *Physical Chemistry of Surfaces*, 3rd ed., p. 411, Wiley, New York (1976); M. J. Rosen, *Surfactants and Interfacial Phenomena*, p. 26, Wiley, New York (1978).

17. D. M. Allen, A. J. Hegarty and D. F. Horne, “Surface Textures of Annealed AISI 304 Stainless Steel Etched by Aqueous Ferric Chloride–Hydrochloric Acid Solutions,” *Trans. Inst. Met. Finish.* **59**, p. 25 (1981).

18. J. E. Prue, “Ion Pairs and Complexes: Free Energies, Enthalpies and Entropies,” *J. Chem. Educ.* **46**, p. 12 (1969).

19. W. Jost, *Diffusion in Solids, Liquids and Gases*, p. 472, Academic Press, New York (1952).

20. W. J. Moore, *Physical Chemistry*, 4th ed., p. 939, Prentice-Hall, Englewood Cliffs, NJ (1972).

21. G. T. Burstein and D. H. Davies, “The Electrochemical Behavior of Scratched Iron Surfaces in Aqueous Solutions,” *J. Electrochem. Soc.* **128**, p. 33 (1981); M. Keddam, O. R. Mattos and H. Takenouti, “Reaction Model for Iron Dissolution Studied by Electrode Impedance,” *J.*

Electrochem. Soc. **128**, p. 257 (1981); S. M. Reshetnikov, "Mechanism of Anodic Dissolution of Iron in Inhibited Hydrochloric Acid Solution," *Zh. Prikl. Khim.* **54**, p. 586 (1981).

22. V. G. Levich, *Physicochemical Hydrodynamics*, Chapters 2 and 3, Prentice-Hall, Englewood Cliffs, NJ (1962).

23. Z. A. Foroulis, *Corros. Sci.* **5**, p. 39 (1965); L. Felloni, *Corros. Sci.* **8**, p. 133 (1968).

24. F. G. Braham, U.S. Patent 2,750,524 (1956); N. Kubo et al., U.S. Patent 3,679,500 (1972); J. J. Frantzen et al., U.S. Patents 3,971,682 (1976) and 4,013,498 (1977); H. H. Bond et al., U.S. Patent 4,142,437 (1978). (Prior art cited in [3]; the resist stencils are made as in A. Goldman et al., U.S. Patent 4,061,529 (1977).)

25. K. Oka et al., "Method for Etching Nickel-Iron Shadow Masks," U.S. Patent 4,420,366 (Dec. 13, 1983). (As described in [26].)

26. R. B. Maynard, J. J. Moscony and M. H. Saunders, "Method for Etching Apertures into a Strip of Nickel-Iron Alloy," U.S. Patent 4,482,426 (Nov. 13, 1984; filed Apr. 2, 1984), RCA Corporation.

27. J. J. Moscony and B. M. Cushman, "Solvent Extraction Method of Separating Ferric Chloride from Nickel Chloride," U.S. Patent 5,718,874 (Feb. 17, 1998), Thomson Consumer Electronics.

28. U.S. Patent 4,396,475 (Aug. 2, 1983), electrolytic removal of nickel in a membrane-divided cell (listed under Stehlik in [26]; its text names W. Faul et al.).

29. M. Gulla, U.S. Patent 3,788,915 (Jan. 29, 1974), electrolytic regeneration of spent etchant.

30. Kim et al., U.S. Patent 4,261,959 (Apr. 14, 1981), solvent extraction of ferric ion with 4-methyl-2-pentanone.

31. H. C. Jeong, D. J. Kim, G. M. Choi and D. J. Kim, "The Effect of Spray Characteristics on the Etching of Invar Alloy with $FeCl_3$ Solution," *Int. J. Precis. Eng. Manuf.* **10**, p. 107 (2009).

32. G. C. Moon, W. K. Choi, S. H. Kim, S. G. Choi and E. S. Lee, "Analysis of the Machining Depth over Time in Wet Etching for Fabrication of Invar Thin Film Shadow Mask," *IOP Conf. Ser.: Mater. Sci. Eng.* **205**, 012021 (2017).

Editor's Notes (2026)

1. **Units.** SI equivalents are given in brackets: 1 psi = 6.895 kPa; 1 microinch = 0.0254 µm; 1 kcal = 4.184 kJ; 1 eu = 1 cal mol^{-1} K^{-1} = 4.184 J mol^{-1} K^{-1}; 1 cP = 1 mPa·s. Heavy-Baumé readings convert to specific gravity by SG = 145/(145 − °Bé) (Fig. E1, right): 32° Bé is SG 1.283, 40° Bé 1.381, 47° Bé 1.480, 54° Bé 1.593 and 57° Bé 1.648. The etch rates in Fig. 15 (2–12 × 10^{-5} g cm^{-2} s^{-1}) correspond to about 1.5–9 µm per minute from each face of the strip in beaker etching.

2. **Exponent in Tables 8 and 11.** The scanned *RCA Review* prints the 32.0° Bé rate constants of Table 8, and the rates in Table 11, as ×10^{-8} cm s^{-1}. Dividing the etch rates of Fig. 15 by the steel density (7.87 g cm^{-3}) gives ×10^{-6} cm s^{-1}, and the axis of the original Arrhenius plot (Fig. 17, log k from −4.9 to −5.3) confirms 10^{-6}. The tables here use 10^{-6}. The 57.0° Bé column (×10^{-7}) is consistent as printed.

3. **Activation parameters recomputed (Fig. E1).** Least-squares fits to Table 8 give E_a = 15.6 kJ/mol (3.72 kcal/mol) and $\Delta H^{\ddagger}$ = 12.8 kJ/mol (3.07 kcal/mol) at 32.0° Bé, and E_a = 48.4 kJ/mol (11.6 kcal/mol) and $\Delta H^{\ddagger}$ = 45.7 kJ/mol (10.9 kcal/mol) at 57.0° Bé, reproducing Table 9. The tabulated $\Delta S^{\ddagger}$ values (−25.3 and −7.2 eu) are reproduced only if the $\ln(k_B/h)$ term of Equation 5 is left out of the intercept, with k in cm s^{-1}. Including it gives −72.6 eu (−304 J mol^{-1} K^{-1}) at 32.0° Bé and −54.3 eu (−227 J mol^{-1} K^{-1}) at 57.0° Bé. Because k here is a heterogeneous rate

constant in cm s^{-1}, the absolute ΔS‡ depends on the choice of units and standard state, so only the *difference* between the two Baumé regions, about 18 eu (76 J mol^{-1} K^{-1}), is meaningful. That difference, together with the fourfold difference in ΔH‡, still supports the change of mechanism argued in Section 4.5.

The perchlorate paper [C] has the same omission. Refitting Table 6 gives E_a = 3.59 and 3.37 kcal/mol and ΔH‡ = 2.97 and 2.74 kcal/mol at 75 and 125 rpm (within error of Table 7), and ΔS‡ = −20.1 and −20.4 eu without the $\ln(k_B/h)$ term, reproducing the published −19.8 and −20.8 eu. With the full Eyring equation, ΔS‡ is about −67.5 eu (−282 J mol^{-1} K^{-1}) at both speeds. Here k_{obs} is a pseudo-first-order constant in s^{-1} that also depends on the area-to-volume ratio of the experiment, so again only comparisons within one apparatus are meaningful. The close match of the perchlorate and low-Baumé chloride values (≈ −20 to −25 eu as reported; ≈ −67 to −73 eu in full) remains good support for a common, transport-limited step.

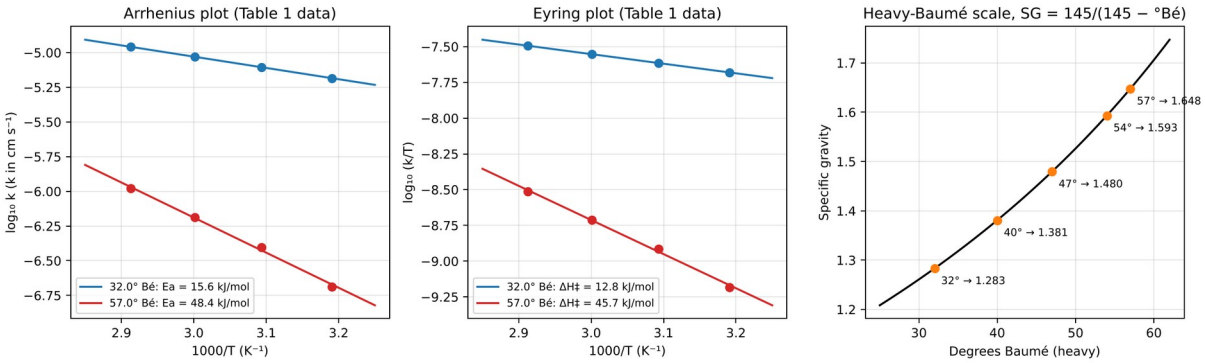


Fig. E1 (new). Left and center: Arrhenius and Eyring plots refitted to the rate constants of Table 8 at 32.0° and 57.0° Bé. Right: heavy-Baumé scale converted to specific gravity.

4. **Smooth-etch rule of thumb.** The transition Baumé rises by about 1° Bé per 10 °C up to 70 °C (Section 4.3). In practical terms the smooth, surface-limited regime that gave the best data-display mask uniformity requires a relatively concentrated etchant (high Baumé, roughly 46° Bé and above at 70–80 °C), at the cost of a lower etch rate and thus lower line speed. This is the trade-off described in Section 5.2.

5. **Patent number.** Reference 2 of [A] prints “U.S. Patent No. 4,309,279 (June 21, 1983).” The patent with that title by Weber and Alleman is US 4,389,279, which matches the date given; the number has been corrected in reference [3].

6. **Mass-transfer cross-check of the two kinetic studies.** For a transport-limited reaction, $k_{obs} = k_m A/V$, where k_m is a mass-transfer coefficient. For the perchlorate runs (V = 500 cm^3; A = 2 × 3.6 × 5.5 = 39.6 cm^2, both faces), $k_{obs} = 6.30 \times 10^{-3}$ and 8.51×10^{-3} min^{-1} give $k_m = 1.3 \times 10^{-3}$ and 1.8×10^{-3} cm/s at 75 and 125 rpm. For a diffusion coefficient of about 6×10^{-6} cm^2/s for Fe^{3+}, these imply diffusion layers about 45 and 34 µm thick, typical of a moderately stirred beaker. In ferric chloride at 32° Bé and 50.1 °C (100 rpm, $[Fe^{3+}] \approx 2.3$ M), the heterogeneous rate of 7.85×10^{-6} cm/s (Table 8) corresponds to an iron flux of 1.1×10^{-6} mol cm^{-2} s^{-1}, or a ferric flux twice that; dividing by the ferric concentration gives an apparent k_m of about 9.6×10^{-4} cm/s. The two studies, at concentrations differing by a factor of about 500, thus give the same mass-transfer coefficient within a factor of two. The lower value in ferric chloride is consistent with its higher viscosity. This quantitative agreement, which neither paper drew out, strengthens the transport-limited interpretation of the low-Baumé chloride etch. The volume exponent of about −0.75 rather than −1 in Fig. 11 is probably hydrodynamic: in the same beaker, a larger volume

changes the liquid depth and the flow pattern around the steel, and so k_m itself. (Calculation in shadow_mask_etch_checks.py.)

7. **Lateral-etch ratio.** [A] gives the lateral etch rate as 60–80% of the depth rate and the smallest single-step opening as about 70% of the strip thickness; the patent [3] gives 50–80% and about the full thickness. The difference probably reflects different aperture types and process settings, and both sources agree that shielding the gun side allows openings smaller than the strip thickness.

8. **Size of the nickel bleed (Fig. E2, center).** Read literally, the overflow rule of [26] is (2.0×10^{-4} g cm^{-2} s^{-1} × exposed mask area in cm^2 ÷ 1.51 g/mL) mL/s. That is a volume of etchant whose mass equals the mass of metal etched, about 0.66 mL of etchant per gram of Invar. A steady-state nickel balance shows this cannot hold the nickel at 5 mol%. Each gram of Invar adds 6.1 mmol Ni and 11.5 mmol Fe, and each milliliter of fresh 49° Bé etchant adds about 4.8 mmol Fe (270 mg/mL [27]). At 0.66 mL/g, the overflow at steady state carries about 30 mol% Ni, close to that of the alloy itself. Holding 5 mol% requires about 22 mL of fresh etchant per gram of Invar etched, some 33 times the printed rate, or equivalent removal of nickel by regeneration. The printed rule is probably a misstatement (perhaps a mass-for-mass replacement of the metal dissolved); in any case it should not be used as a design figure. The order of magnitude is consistent with [27], where spent etchant is replaced at about 5% nickel (the example etchant is 5.4 wt%, 5.2 mol%). (Calculation in shadow_mask_etch_checks.py.)

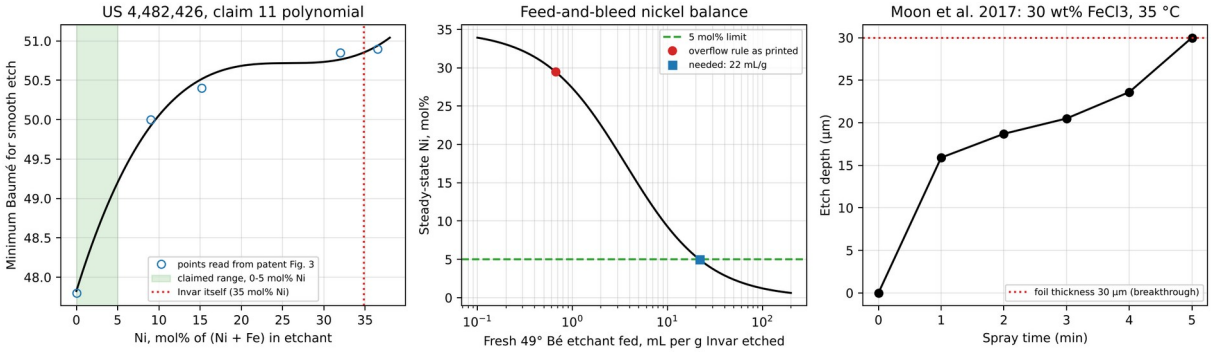


Fig. E2 (new). Left: minimum Baumé for smooth etch of Invar against nickel content (claim 11 polynomial of [26], with points read from Fig. 30). Center: steady-state nickel content against the feed of fresh 49° Bé etchant per gram of Invar etched. Right: etch depth against time in 30 µm Invar foil, from Moon et al. [32].

9. **Interpreting the 2017 Invar data.** Moon et al. [32] attribute the fast first minute (15.9 µm) and the slower later rate (about 2.6 µm/min) to a change from anisotropic to isotropic etching. The kinetics of Section 4 suggest a simpler cause. In their dilute, low-temperature etchant (30 wt % $FeCl_3$ is about 1.29 g/mL, or about 33° Bé), the reaction is transport-limited, and as the cavity deepens beneath the resist opening, fresh etchant reaches the bottom less easily, so the depth rate falls. The jump from 23.6 µm to breakthrough between 4 and 5 minutes is consistent with the narrowing remaining web being opened by the spray. On the RCA results, these conditions would give a rough etch (Figs. 23, 29). Their Equation (2) is printed as $Ni + 2FeCl_3 \rightarrow 2FeCl_2 + NiCl$ and should read $NiCl_2$, as in Section 6.1. Their reported hole entrance (119 × 91.6 µm) compared with the 120 × 80 µm resist opening implies little growth in the long direction and about 12 µm in the short direction. Because the long-direction value is not easily reconciled with lateral etching, it should be checked against their SEM images.

10. **Invar transition and the chloro-species model.** The temperature independence of the smooth/rough transition for Invar (Fig. 29), unlike that of low-carbon steel (Fig. 23), is not

explained in [26]. In the picture of Section 4.5, the transition marks the point where the etch changes from transport-limited to surface-limited as $FeCl_4^-$ becomes predominant. Nickel or a nickel-rich surface layer on the dissolving alloy may control the surface step for Invar, making the crossover depend mainly on etchant composition. That nickel ion in solution raises the transition Baumé (Fig. 30) is consistent with nickel’s taking part at the surface. This is an editor’s suggestion, not a finding of the sources.